JOURNAL OF EARTHQUAKE ENGINEERING
2023, VOL. 27, NO. 16, 4664–4693
https://doi.org/10.1080/13632469.2023.2189978

Taylor & Francis
Taylor & Francis Group

Experimental Parametric Study and Phenomenological Modeling of a Deformable Rolling Seismic Isolator

Antonios A. Katsamakas and Michalis F. Vassiliou

Institute of Structural Engineering, ETH Zurich, Zurich, Switzerland

ABSTRACT

This paper presents an extensive experimental study of a low-cost, high-performance seismic isolator comprising a deformable sphere rolling on concrete surfaces. Polyurethane spheres, with and without steel core, rolling on flat or spherical concrete plates, are investigated. Lateral cyclic tests under large displacements demonstrated a rolling friction coefficient between 3.7% and 7.1%. When tested in a shake table under 1170 ground motions, the isolators substantially reduced the acceleration transmitted to the superstructure (to less than 0.15 g) while maintaining reasonable peak and negligible residual displacements. A phenomenological model was calibrated on the lateral cyclic tests and predicted the shake table tests with reasonable accuracy.

ARTICLE HISTORY
Received 20 June 2022
Revised 22 February 2023
Accepted 7 March 2023

KEYWORDS
Seismic isolation; earthquake engineering for the developing world; rolling bearings; rubber bearings; seismic testing; numerical modeling

1. Introduction

Earthquakes are a global phenomenon; however, their impact, both in terms of fatalities and economic loss, is mainly concentrated in the low-income countries of the globe (Fink et al. 2017). The main reason is the high vulnerability of the structures in these regions since modern structural codes are too expensive to be followed. Therefore, there is an urgent need for proposing and implementing earthquake-resistant methods applicable to low-income countries of high seismic risk. The suggested methods should a) be affordable; b) be adaptable to local construction practices; c) rely on quality control procedures that can be followed in the countries of interest; d) not grossly rely on imports of construction materials.

Seismic isolation is a well-established method of seismic protection of structures. Its basic concept lies in the uncoupling of the superstructure from the ground motion, typically by using a sliding layer or a layer with low lateral stiffness. This layer should be able to carry the gravity loads and provide sufficient energy dissipation to limit maximum displacements. Due to its high cost, in low-income regions of the globe, seismic isolation is mainly implemented in projects of very high importance. The high cost originates from: a) the cost of each bearing, which can be higher than $10k, whereas a large number of bearings is required on each application, b) the cost of the additional, thick, heavily reinforced concrete isolation slab, which serves as a diaphragm and is typically constructed at the isolation level, and c) the implementation cost.

Seismic isolators could be distinguished into three main categories, namely: a) Flexible rubber bearings; b) Sliding bearings; c) Rolling bearings. Over the last decades, there have been studies suggesting alternative, reduced-cost devices based on all these three categories.

A rubber isolator using fiber reinforcement, instead of steel shims that are used in conventional rubber isolators, the "Fiber Reinforced Elastomeric Isolator (FREI)," has been proposed and studied

CONTACT Antonios A. Katsamakas katsamakas@ibk.baug.ethz.ch Institute of Structural Engineering, ETH Zurich, Stefano Francini Platz 5, Zurich CH-8097, Switzerland

(Das, Deb, and Dutta 2016; De Domenico, Losanno, and Vaiana 2023; Kelly and Calabrese 2012; Kelly and Takhirov 2001; Konstantinidis and Kelly 2012; Konstantinidis, Kelly, and Makris 2008; Osgooei, Tait, and Konstantinidis 2014; Ruano and Strauss 2018; Russo, Pauletta, and Cortesia 2013; Toopchi-nezhad, Tait, and Drysdale 2009; Tran et al. 2020; Van Engelen, Konstantinidis, and Tait 2016; Van Engelen, Tait, and Konstantinidis 2014). FREIs remain too stiff to isolate lightweight (i.e. one or two-story) residential buildings. Seismic isolation bearings based on sliding require polished metals and Teflon surfaces for the low-friction sliding interfaces. Thus, they are, in principle, not affordable in low-income countries. In previous studies, Jampole et al. (2014, 2016) and Swensen (2014) have studied high-density polyethylene sliders on galvanized steel, with these materials serving as the reduced-cost alternatives to conventional steel-Teflon interfaces. The isolators were efficient, and the system could be viable in places where galvanized steel and timber are available. However, communication with engineers in Peru (Prof. Marcial Blondet, video conference, February 10, 2021) and Cuba (Dr. Dario Candebat Sánchez, telephone conversation, February 2, 2021) has revealed that, in many low-income countries, these materials are not available at a low cost. Brito, Ishibashi, and Akiyama (2019, 2020, 2021) used concrete-steel friction interfaces and concave surfaces of varying geometry as inexpensive bearings for bridges. Restoring force was provided through gravity, and the measured friction coefficient was in the range of 0.3, which, even though it is higher than the friction coefficient of common Teflon-steel bearings, could be an improvement in comparison to conventional design.

Tsiavos et al. (2019, 2020a, 2020b, 2021) have suggested the use of sand/rubber mixtures or of sand grains enclosed in PVC sheets as isolation layers below the foundation slab. Experimental results show that these sliding-based isolation systems act as a fuse, capping the maximum transmitted acceleration at the values of the sliding friction coefficient. Such a solution lacks restoring force. Under the presence of unavoidable imperfections, this can lead to excessive maximum and residual displacements (Constantinou, Mokha, and Reinhorn 1991; Tsopelas and Constantinou 1997).

There have been numerous isolation systems based on rolling (Harvey 2016; Harvey and Gavin 2014; Harvey and Kelly 2016; Harvey, Zéhil, and Gavin 2014; Jangid and Londhe 1998; Lee et al. 2010; Lin and Hone 1993; Ou, Song, and Lee 2010; Zhou et al. 1998). The vast majority of them uses steel bearings rolling on steel surfaces; hence, they may be too expensive to apply in low-income countries. Aiming at increased energy dissipation and avoidance of failure at the contact areas (Foti 2019; Foti and Kelly 1996; Katsamakas et al. 2021a, 2021b, 2022; Menga, Bottiglione, and Carbone 2019; Menga, Foti, and Carbone 2017; Zéhil and Gavin 2013, 2014) have suggested the use of rubber (or, in general, viscoelastic materials) at the contact interfaces.

Based on the work of Cui, Bruneau, and Constantinou (2012), one of the most recent suggestions for seismic isolation of lightweight residential structures, that could be applicable to the developing world, has been the Spherical Deformable Rolling Seismic Isolator (SDRSI) by Cilsalar and Constantinou (2019a, 2019b, 2020), an analogue of a Friction Pendulum System (FPS), based on a deformable elastomeric sphere with a diameter of 254 mm rolling on a spherical (concave) concrete surface (Fig. 1, left, middle). The exact cost for the implementation of such a system lies beyond the

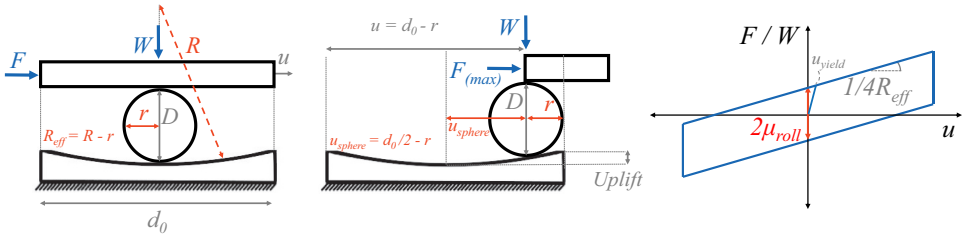

Figure 1. Rigid body model for rolling seismic isolators. Left, isolator under compressive load and zero lateral displacement; middle, isolator under compressive load and maximum lateral displacement; right, bilinear force-displacement plot.

scope of this study, remains to be determined, and would depend on the region of implementation. Two variations of SDRSI were tested by Cilsalar and Constantinou (2019a, 2019b, 2020): one using solid Polyurethane (PU) spheres and one with a steel core, to reduce creep and make the system stiffer. Spheres of shore hardness 95A and 62D were tested.

Approximating the behavior of such a system using a simplified model of a rigid sphere rolling on a rigid spherical surface is tempting as it provides FPS-like and easy-to-use equations describing the force-deformation loops (Fig. 1, right). Then, a Bouc-Wen model can be used to describe the isolator (Nagarajaiah, Reinhorn, and Constantinou 1991; Wen 1975). However, the tests of Cilsalar and Constantinou (2019a, 2019b, 2020) showed a significant deviation between experimental results and rigid body model predictions: The loops of the tested isolators were 2–3 times stiffer than analytical predictions. In fact, in some of the tests, characterizing the experimental loops as "bilinear" (even if a larger stiffness is used) seems inadequate. Notably, the tests of Cilsalar and Constantinou (2019a, 2019b, 2020) involved displacements up to 125 mm that correspond to a sphere rolling of 0.5 rad. Therefore, the sphere experienced much less than half of a full rotation. Note that throughout this paper, the term "bilinear" is used in a general form to also include systems of infinite pre-yield or zero post-yield stiffness.

Trying to explain this apparent increase in stiffness, Katsamakas et al. (2021a, 2022) tested smaller spheres (100 mm diameter, shore hardness 85A, without a steel core) to displacements of 100 mm. This corresponds to 1 rad of sphere rotation. They measured the vertical displacement of the setup when rolling the sphere under constant compressive load to observe a significant vertical motion even when rolling on perfectly flat surfaces. They concluded that the apparent stiffness increase observed by Cilsalar and Constantinou (2019a) is due to residual "creep" deformation of the sphere under vertical compressive load that results in essentially rolling an oval-shaped sphere, rather than a perfect sphere (Fig. 2). Therefore:

a) The loops significantly deviate from a bilinear shape, especially under larger sphere rotations;
b) The tangent stiffness of the isolators is initially larger than the rigid body model, but is expected to decrease for larger displacements (Katsamakas et al. 2022). Overall, the behavior of such a system is more complicated than a bilinear model.

Moreover, the behavior of the sphere material cannot be predicted by a linear viscoelastic model. Tests show that the observed creep deformation is not reversible when the compressive load is removed; that is, there is damage. Notably, when tennis balls filled with cement paste were tested as an alternative device, the tests showed a bilinear behavior (Katsamakas et al. 2021b), due to the small thickness of the rubber shell of the tennis ball.

Aiming at better understanding the mechanics of SDRSIs as low-cost, high-performance seismic isolators, this paper presents extensive experimental tests and phenomenological modeling of PU spheres of shore 95A, with and without a steel core, under design-level lateral displacements. Testing under design displacements is particularly important due to the strongly nonlinear behavior of the

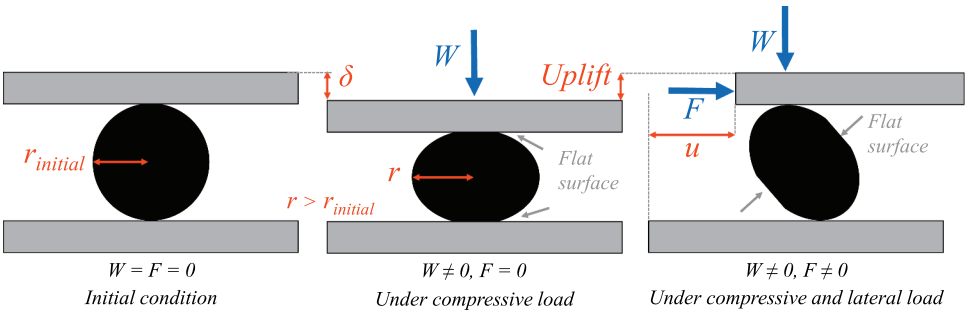

Figure 2. Left, initial condition of the spherical isolator; middle, isolator under compressive load with evident compressive displacement; right, isolator under compressive and lateral load, with evident uplift.

system that had been previously assumed to be quasi-bilinear (Cilsalar and Constantinou 2019a). Moreover, this paper offers a phenomenological model to describe the behavior of the isolator. To this end, following the introductory section, the second section describes the isolator. The third section discusses its proposed use in an effort to justify the design of the tests. Section 4 discusses the experimental setup. Section 5 presents compressive tests of the elastomeric balls. Sections 6 and 7 discuss lateral cyclic tests and proof-of-concept shake table tests. Finally, section 8 proposes a phenomenological model to describe the lateral behavior of the isolator.

2. Description of the Proposed Isolator and Rigid-Body Equations

The proposed seismic isolator comprises a deformable PU sphere that rolls between two concrete surfaces. Cilsalar and Constantinou (2019a, 2019b) claim that one of these two concrete plates should be spherical to guarantee gravitational restoring force to the system. Placing the spherical plate above or below the rolling sphere has no influence on the response of the system; therefore, a designer would have to consider only practical issues (e.g. rainwater drainage and easiness of construction) for this decision. The use of two spherical plates (i.e. both above and below the rolling sphere) is neither suggested nor tested since this configuration is more complicated and expensive to construct, while it does not offer an advantage in size (Cilsalar and Constantinou 2019a). The use of two flat plates would lead to a system without restoring force – at least according to the rigid body model. The need of a restoring mechanism in seismic isolation systems is crucial in order to control excessive peak and residual displacements. These displacements will be significantly amplified in the case of inevitable accidental inclination of the isolation level (net inclination of the isolation level in one direction) because of accumulation of displacements (Constantinou, Mokha, and Reinhorn 1991; Tsopelas and Constantinou 1997). In the present study, configurations with two flat plates are also tested, in order to characterize the behavior of the rolling sphere without the curvature of the concrete surface influencing the response.

The shape of the spherical surface (radius of curvature and displacement capacity) could be tailored and optimized for each application, similarly to sliding systems with spherical surfaces. The design procedure could start with the rigid body approximation, where the deformability of the sphere is not considered. Then, the force-displacement relation that describes the lateral response of the system is (Cilsalar and Constantinou 2019a):

$$F = \frac{W}{4R_{eff}}u + \mu_{roll}Wsign(\dot{u}) \tag{1}$$

where F is the horizontal force applied to the isolator, W is the vertical force (weight) applied to the isolator, u is the lateral displacement of the isolator, δ is the compressive displacement under load W, $R_{eff} = R - r$, R is the radius of curvature of the spherical concrete plate and $r = D/2$ is the radius of the rolling sphere (Fig. 1). The quantity $\frac{W}{4R_{eff}}u$ is the gravitational restoring force of the system. The "4" factor in the denominator is noteworthy, since, the rolling isolator is 4 times more "flexible" than a Friction Pendulum System (FPS) with the same radius of curvature (R). This is because the translational displacement of the sphere (u_{sphere}) is equal to half of the displacement of the isolator (u); hence, $u_{sphere} = u/2$. The isolation period of the system is defined as $2\pi\sqrt{\frac{4R_{eff}}{g}}$. The μ_{roll} term is the rolling friction coefficient of the system and is a macroscopic term that describes the initiation of rolling motion. More on the rolling friction is discussed in section 6. The displacement capacity of the isolator is d_o - D (Fig. 1).

The equation that correlates the rotation of the rolling sphere (θ) with the displacement of the isolator (u) is (Eq. (2)):

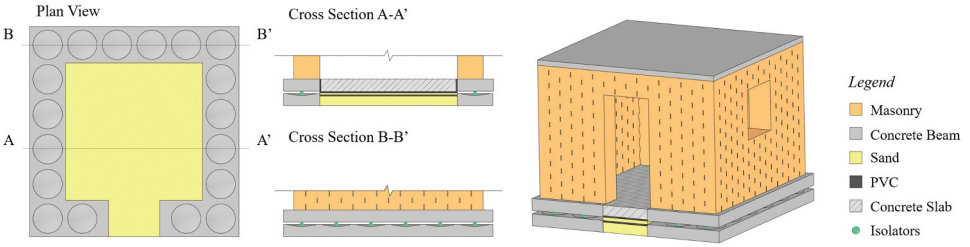

Figure 3. Representation of a potential application of deformable rolling isolators in low-rise masonry buildings.

$$\theta = \frac{u}{2} \times \frac{1}{r} \tag{2}$$

3. Proposed Use of the Isolator

A potential application of the system proposed in the present study could be in one- or two-story masonry houses, in countries where reinforced concrete is not available or is too expensive. In these regions, the construction of seismically isolated masonry houses could be a viable solution for earthquake-resistant structures. For example, South East Cuba, which lies close to the fault that caused the 2010 Haiti catastrophe, has a 10% in 50 years PGA equal to 0.33 g (Norma Cubana NC46 2017), which essentially prohibits the use of masonry – which is the only easily available material. The example of Santiago, Cuba is used in the present study since it is considered as representative of regions of high seismicity and low availability of construction materials. Similar (or higher) seismicity and analogous lack of resources can be found in many countries in Latin America, in Asia, and Africa.

Even though the system-level response of a structure isolated with SDRSIs lies outside the scope of this paper, this section describes the envisaged use of the isolation system, so that the compressive load protocol and the size of the spheres used in the presented test campaign is justified.

Communication with practicing engineers from Cuba (Dr. Dario Candebat Sánchez, telephone conversation, February 2, 2021) and Peru (Prof. Marcial Blondet, telephone conversation, February 10, 2021) has unveiled that, at least in their countries, and probably in other countries of similar construction practices and income, seismic isolation cannot be financially viable for low-rise buildings because of the cost of the extra and heavily reinforced slab at the isolation level. Unless the cost of this slab is reduced, seismic isolation cannot be financially competitive, even if the isolation system is provided at zero cost.

Therefore, this paper suggests the combination of the systems of Cilsalar and Constantinou (2019a, 2019b, 2020) and of the one suggested by Tsiavos et al. (2019, 2020a, 2020b), for the isolation of 1–2 story masonry houses (Fig. 3). The walls are supported on RC connecting beams that serve as the upper rolling surface of the isolators. The rolling isolators carry the weight of the structure. The low cost of each isolator allows for placing multiple of them in closely spaced distances. The reinforcement of the RC beams is controlled by the distance between the isolators. Hence, the optimal number of isolators should be determined by optimizing the total cost of the SDRSIs and the connecting beam. The ground floor slab will be continuously supported by two sheets of PVC (with some sand in between) that provide a coefficient of friction at the order of 0.2 – but no restoring force. Such a continuous support allows for reducing the thickness of the slab and for providing minimal (if any) reinforcement, making its cost similar to the cost of the cleaning concrete layer that is used in fixed base structures. Therefore, the cost originating from the concrete elements is expected to be significantly reduced.

Because of the SDRSIs, a horizontal motion of the beams also causes a vertical one. Therefore, two options exist for the connection between the slab: a) It could be monolithic (not shown in Fig. 3) or b)

a PVC joint could be used that would allow the vertical motion of the beams while the slab only moves horizontally (shown in Fig. 3). In the former case, the slab will lose the continuous vertical support and might crack (without causing any life threat). In the latter case, the cover of the slab (be it tiles, mosaic or any other material local construction uses) will fail only along the joints.

4. Experimental Setup

4.1. Testing Equipment and Instrumentation

The setup has been previously described in Katsamakas et al. (2022) but is briefly described in this section for reasons of completeness. Both the lateral cyclic and the shake-table tests were performed using the 1 degree-of-freedom shake table of ETH Zurich (Bachmann et al. 1999). Even though the shake table was used as an actuator for the cyclic tests, this paper uses the term "shake table tests" only for the tests where the shake table applied ground motions and was not merely used as an actuator to apply lateral cyclic loads.

The experimental setup, both for the lateral cyclic and the shake table tests (Fig. 4), comprises 4 isolators. An isolator comprises a PU sphere rolling between two concrete plates.

In all tested configurations, the lower concrete plates were flat. The upper concrete plates were either flat ("flat configurations") or spherical ("spherical configurations"). The lower concrete plates were fixed to the shake table platen, whereas the upper ones were mounted on a steel slab with a thickness of 30 mm.

During the lateral cyclic tests, the motion of the top-slab parallel to the x-axis was restrained by two rigid struts fixed to a rigid column. Restrainers prevented the slab from moving out of plane (y-axis) and from rotating around the z-axis (Fig. 4). To minimize friction between the slab and the stoppers, all surfaces where contact was possible were covered with Teflon sheets. During cyclic testing, the shake table applied a sinusoidal motion to the bottom concrete plates, the top plates were kept in place

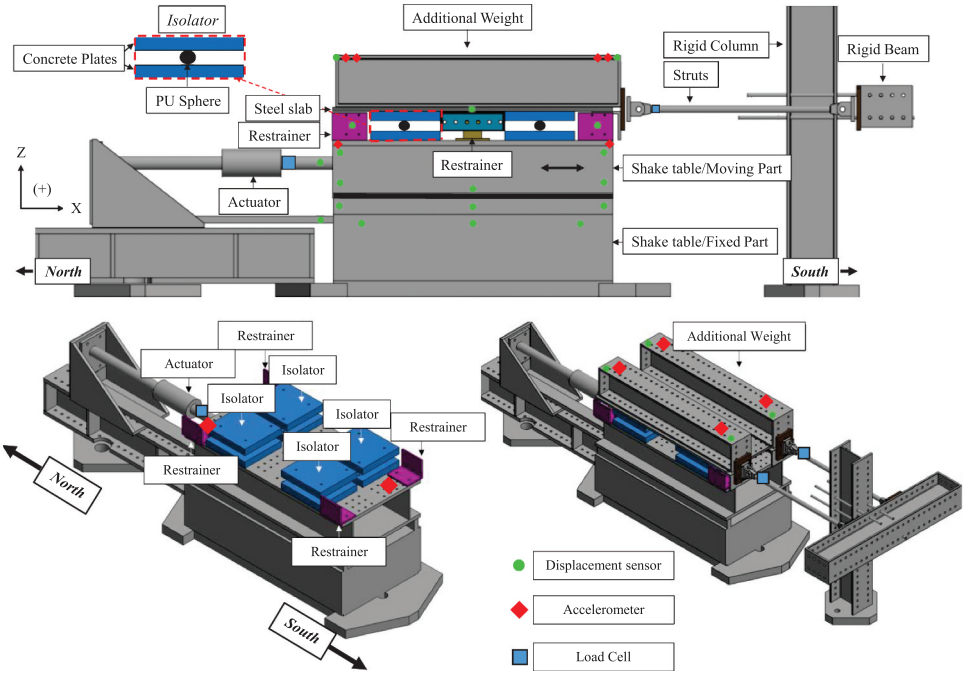

Figure 4. Representation of the experimental setup. Green circles, red diamonds, and blue squares show the location of the triaxial displacement sensors, the triaxial accelerometers and the uniaxial load cells, respectively.

by the rods, and shearing of the isolators was achieved. The vertical load (emulating the weight of the isolated superstructure) was applied by fixing masses on top of the steel slab. For the shake table tests, the steel rods were removed, and the steel slab was free to move along the x-axis.

Four three-dimensional accelerometers (one on each corner) were placed on top of the steel slab. Two more three-dimensional accelerometers were placed on the shake table platen (red diamonds in Fig. 4). The struts that hold the steel diaphragm in place were equipped with load cells, measuring the reaction force of the isolators to the applied motion during the lateral cyclic tests. Another load cell was placed at the actuator that drives the shake table. The sampling rate of the accelerometers and the load cells was 1200 Hz. The movement of the shake table and the superstructure was measured using an NDI Optotrak Certus camera. A total of 22 infrared-emitting diode markers were used to track the motion of the superstructure and the steel slab (green circles in Fig. 4). The NDI system had an accuracy of 0.1 mm and a sampling rate of 60 Hz.

The shake-table setup is idealized since it does not account (or partially accounts) for the following effects:

(a) The overturning moment of the building. The height of the center of mass in the shake table tests was approximately 30% ($W = 4.74$kN) or 65% ($W = 3.23$kN) lower than what an undistorted physical model of a one-story masonry building would require. A larger overturning moment would affect the normal force applied to the isolators, hence, the lateral response. Under triaxial excitation, it could also induce torsion (Almazán and de la Llera 2003).
(b) The three-dimensional nature of the ground motions, since the applied ground motion is one-directional. A bi-directional horizontal excitation would result in different isolator displacements. Moreover, the vertical ground motion is expected to affect the response of gravity-based isolators, as the ones described in the present study.
(c) The flexibility and the finite strength of the superstructure. This flexibility would affect both the response of the isolators and the superstructure.
(d) The behavior of the isolators when the restrainer is engaged (i.e. response at extreme lateral displacements).

The scope of the shake-table study presented herein is to provide:

(a) A detailed description of the dynamic response of the isolators under (one-dimensional) dynamic excitation to validate the lateral cyclic tests.
(b) An extensive experimental parametric analysis to study the effect of the vertical load, the type of the isolator, and the curvature of the concrete plates.
(c) Experimental results to validate the dynamic response predicted by the phenomenological model (described in subsequent section). The only previous study to test SDRSIs under shake-table excitations is the one by Katsamakas et al. (2022), but these tests used more flexible spheres that resulted in larger friction coefficients and, thus, higher superstructure accelerations.
(d) Results that would be useful for the preliminary design of a practical application or for the design of more detailed shake-table tests, which would alleviate the limitations of the present study, including the three-dimensional nature of the excitation and the modeling of the superstructure.

4.2. Materials

Three types of spheres were tested, namely, solid spheres with a diameter of 100 mm, spheres with a diameter of 100 mm and a 50 mm steel core inside (spheres 100/50 mm), and spheres with a diameter of 80 mm and a 50 mm steel core inside (spheres 80/50 mm). The spheres were made of PU with a shore hardness of 95A. The steel core was made of Gcr15 steel with $f_y = 415$ MPa and $f_u = 520$ MPa,

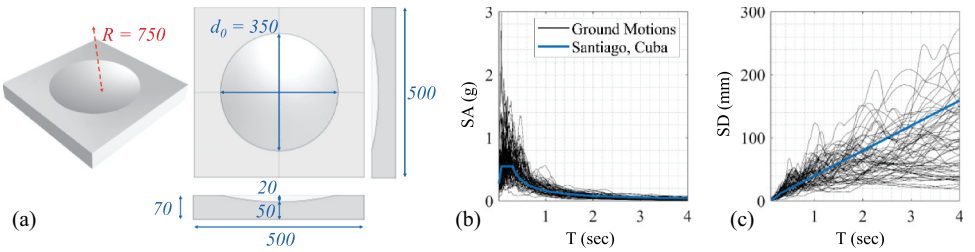

Figure 5. (a) Shape and dimensions of the utilized spherical concrete plates (in mm); elastic response spectra of the applied ground motions and design spectrum of Santiago, Cuba (in model scale). (b) pseudo-accelerations; (c) displacements.

according to the manufacturer. The cost of 100 mm, 100/50 mm, and 80/50 mm spheres was $23, $30, and $25 per piece, respectively. Note that for larger orders, these amounts are expected to be significantly reduced.

A commercial M15 concrete mix, with a maximum aggregate size of 4 mm, was selected for the construction of the concrete plates. Fig. 5 shows the dimensions of the spherical concrete plates. The material for each of these plates costs $6. The plates were unreinforced to model practical applications where only minimal reinforcement would be used (e.g. to control shrinkage cracking). The mean compressive and flexural strength of the concrete mix was 27.6 MPa and 4.6 MPa, respectively, tested according to EN 1993-11 (1993). The exact manufacturing procedure of the spherical surfaces in a low-income country is a topic that should be resolved in collaboration with practicing engineers from these countries. Communication with engineers from Cuba revealed that they could be locally constructed (Dr. Dario Candebat Sánchez, telephone conversation, February 2, 2021).

4.3. Similitude Laws and Tested Configurations

Due to the setup limitations, a geometric scale factor of 0.5 ($S_L = 0.5$) was chosen for the shake table tests. Therefore, to ensure similitude of stresses, the force and time scaling factors are $S_F = 0.25$ and $S_T = 0.707$, respectively. Table 1 summarizes the scaling laws, whereas Table 2 shows the values of the

Table 1. Summary of scaling laws for reduced-scale physical modeling (artificial mass simulation). In the present study $S_L = 0.5$.

Quantity	Model/prototype
Length	S_L
Area	S_L^2
Vertical Load	S_L^2
Time	$S_L^{0.5}$
Frequency	$S_L^{-0.5}$
Acceleration	1

Table 2. Summary of the main quantities of the experimental model and the corresponding prototype structure.

Quantity	Model Scale	Prototype Scale
Radius of spherical concrete plates (R)	750 mm	1500 mm
Eigenperiod of spherical concrete plates	3.44 sec	4.87 sec
Plan view diameter of the spherical isolator	350 mm	700 mm
Diameter of rolling spheres	100 mm	200 mm
	100/50 mm	200/100 mm
	80/50 mm	160/100 mm
Vertical load	2.08, 3.23, 4.74, 8 kN	8.32, 12.92, 18.96, 32 kN
Amplitude of cyclic test	±115 mm	±230 mm
Equivalent amplitude of one-sided cyclic tests	±230 mm	±460 mm

Table 3. Summary of the tested configurations.

		Type of Rolling Spheres (mm)		
Weight per sphere (kN)	Concrete Plates	*100*	*100/50*	*80/50*
2.08	Flat	Shake table	Shake table	Cyclic/Shake table
	Spherical	Cyclic/Shake table	Cyclic/Shake table	Cyclic/Shake table
3.23	Flat	Cyclic/Shake table	Cyclic/Shake table	Cyclic/Shake table
	Spherical	Cyclic/Shake table	Cyclic/Shake table	Cyclic/Shake table
4.74	Flat	Cyclic/Shake table	Cyclic/Shake table	Cyclic/Shake table
	Spherical	Cyclic/Shake table	Cyclic/Shake table	Shake table
8	Flat	Cyclic	Cyclic	Cyclic

main design parameters in the model and prototype scale. In the plane view, the diameter of the spherical concrete plate was 350 mm (Fig. 5). The radius of curvature of the spherical concrete plates (R) was $R = 750$ mm. Neglecting the size of the sphere and based on Eq. (1) this would give an isolation period of 3.44 s and 4.8 s in the model and the prototype scale, respectively. This rather high isolation period was selected based on the conclusions of previous studies (Cilsalar and Constantinou 2019a) where it was suggested that Eq. (1) significantly underpredicts the stiffness of the bearing.

To calculate the compressive load that should be applied, a modern unconfined masonry house in Cuba was considered (Katsamakas et al. 2022), resulting in a gravity load per isolator of 11 kN (i.e. 2.75 kN in the model scale). The value is low compared to other studies on seismic isolators, because the proposed design targets one story houses and requires multiple isolators.

Four compressive loads (2.08 kN, 3.23 kN, 4.74 kN, or 8 kN per sphere – model scale) under 2 rolling surface curvatures (flat and spherical) were planned for all 3 spheres. The minimum tested load (2.08 kN) is slightly lower than the design load of 2.75 kN to account for cases where, due to overturning moment, limited decompression is observed. Contrariwise, the maximum tested load (8 kN) significantly exceeds the design load to account for the additional compressive force due to overturning moment, or to investigate the response of the isolators considering that the tested sphere diameters are full-scale models with a slightly lower load. It is noted that, in all shake-table tests, before the application of the seismic motion, the isolators were subjected to sustained compressive (creep) load for 7 days so that their compressive creep displacements were concluded.

Due to limitations of the experimental setup and safety concerns, some configurations were not tested. Tables 3 and 4 list the tested configurations. The actuator of the shake table had a stroke of 230 mm. Therefore, two types of cyclic tests were performed: a) between −115 and +115 mm and b) between 0 and +230 mm and 0 and −230 mm.

The shake table tests were performed under an ensemble of 61 different ground motions, selected from all three different categories of FEMA P695 (2009) (i.e. far-field, near-field pulse-like, and near-field non-pulse-like). All ground motions were scaled by $\sqrt{2}$ in the frequency domain, since the tested model corresponds to a half-scale ($S_L = 0.5$) representation of a prototype structure (Table 1). Subsequently, all ground motions were acceleration-scaled so that they comply with the capacity of the shake table (Bachmann et al. 1999), with the acceleration scaling factor ranging from 0.7 to 1. Fig. 5b,c plots the elastic response spectra of the pseudo-accelerations and displacements of the ground motions used in the shake table tests, together with the design spectrum for a site in Santiago, Cuba (model scale), assuming soil type C, 5% damping and a return period of 475 years. Out of the 61

Table 4. Summary of the performed cyclic tests.

Sphere type	Curvature of Concrete Plates	Vertical load per sphere (kN)	Cyclic test performed
100 mm	Flat	2.08/3.23/4.74/8	0/+230, 0/-230, −115/+115
	Spherical	2.08/3.23/4.74	
100/50 mm	Flat	2.08/3.23/4.74/8	
	Spherical	2.08/3.23/4.74	
80/50 mm	Flat	2.08/3.23/4.74/8	
	Spherical	2.08/3.23/4.74	

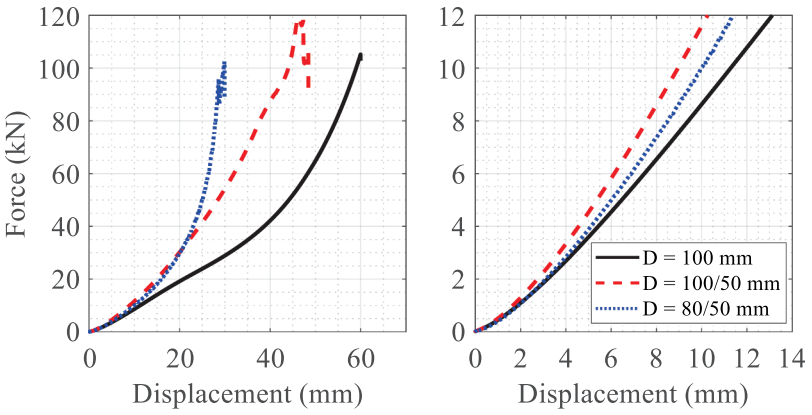

Figure 6. Compression testing results. Left: force-displacement; right: force-displacement (detail).

ground motions, 35 were far-field motions, 13 were near-field pulse-like motions, and 13 were near-field non-pulse-like motions. The PGA, PGV, and PGD values of the far-field motions ranged between 0.07 and 0.40 g, 99–200 mm/sec, and 21.8–104.9 mm, respectively. The PGA, PGV, and PGD values of near-field pulse-like motions ranged between 0.16–0.79 g, 148–200 mm/sec, and 12.7–127.7 mm, respectively. The PGA, PGV, and PGD values of near-field non-pulse-like motions ranged between 0.16–0.60 g, 145–200 mm/sec, and 15.1–105.6 mm, respectively. All PGA, PGV, and PGD values are given in the model scale.

Details about the ground motions used and the scaling factor applied can be found in (Katsamakas et al. 2022). This paper used the same ground motions and applied the same scaling factors.

5. Compressive Response

The spheres were first subjected to monotonic uniaxial compression, at a displacement rate of 0.33 mm/sec and 0.27 mm/sec for the spheres with an external diameter of $D = 100$ mm and $D = 80$ mm, respectively (Katsamakas et al. 2022). The test was terminated when $\delta/D = 0.6$ (where δ is the compressive displacement), or when the spheres reached compressive failure, defined as a 20% drop of the maximum compressive load. The maximum load that the spheres sustained under these testing conditions was 105.2 kN, 118.8 kN, and 102.5 kN for the 100 mm, 100/50 mm, and 80/50 mm spheres, respectively (Fig. 6). These load levels are substantially higher than the ones that the spheres would have to sustain in a practical application (Section 3). Thus, the loss of vertical load-bearing capacity of the spheres is not the critical design parameter. It is worth noting that failure was reached only for the spheres with a steel core, whereas for the solid spheres, the force-deformation relationship increased monotonically. This does not mean that the solid spheres were not damaged: After removing the load, there was a permanent deformation of the solid spheres that was not recovered even after several weeks. Therefore, no linear viscous model can describe its behavior, even if more than one branch is used (Generalized Maxwell Model).

Table 5. Compressive Tangent Stiffness of the spherical isolators at different load levels.

Compressive Tangent Stiffness (kN/mm)			
Sphere type	100 mm	100/50 mm	80/50 mm
Stiffness at 2.75 kN	0.87	1.09	0.97
Stiffness at 11 kN	1.07	1.52	1.58

Considering the tested spheres as 1:2 scaled models of prototype spheres, the tangent vertical stiffness at 2.75 kN is of interest and is given in Table 5 (in model scale). Table 5 also offers the tangent stiffness at 11 kN, which is the design compressive load in the prototype scale (in case spheres of the tested size are directly used for design at a prototype scale).

As expected, a comparison of the 100 and 100/50 spheres shows that the presence of a steel core increases the stiffness of the sphere. A comparison between the 100/50 and 80/50 sphere (Fig. 6) shows that the secant stiffness of the 100/50 sphere is larger up to loads of 30 kN (which are the loads of interest), but for larger loads, the 80/50 sphere becomes stiffer. This can be attributed to excessive compression of the rubber cover in the 80/50 layer that results into strains in the PU in a strain region where it stiffens. A detailed explanation of this observation would require more tests and a refined numerical model using a calibrated constitutive law, and thus, lies beyond the scope of this paper.

6. Lateral Cyclic Response

All configurations were left to creep for 7 days (which was enough for the creep to be concluded) and then subjected to the following sequence of lateral cyclic tests:

(1) Cyclic ("0/+230") tests with the shake table used as an actuator and applying 3 loops of a sinusoidal motion to the bottom concrete plate between zero and +230 mm (that is, $u(t) = 115 \times (1 - \cos(2\pi f \times t))$.
(2) Cyclic ("0/-230") tests with a motion between zero and −230 mm (that is, $u(t) = -115 \times (1 - \cos(2\pi f \times t))$.
(3) Cyclic ("±115 mm") tests comprising five loops of a sinusoid with an amplitude of 115 mm (that is $u(t) = 115 \times \sin(2\pi f \times t)$)

The excitation frequency of all cyclic tests was $f = 0.2$ Hz, which is similar to the one used by Cilsalar and Constantinou (2019a, 2019b). A further increase of the frequency would be of interest in a future experimental investigation, but is not considered herein due to limitations of the used setup. Fig. 7 (left) shows the displacement of the shake table related to the above protocols, as recorded during the tests.

Fig. 7 (right) compares the force-displacement loops obtained from the "0/+230" and the "0/-230" tests and the corresponding plot from the "±115 mm" test. It is evident that the plots overlap, meaning that the equivalent "±230 mm" test (comprising the "0/+230" and the "0/-230" plots) is the extension of the "±115 mm" test. Therefore, from now on, only the equivalent "±230 mm" plots are presented.

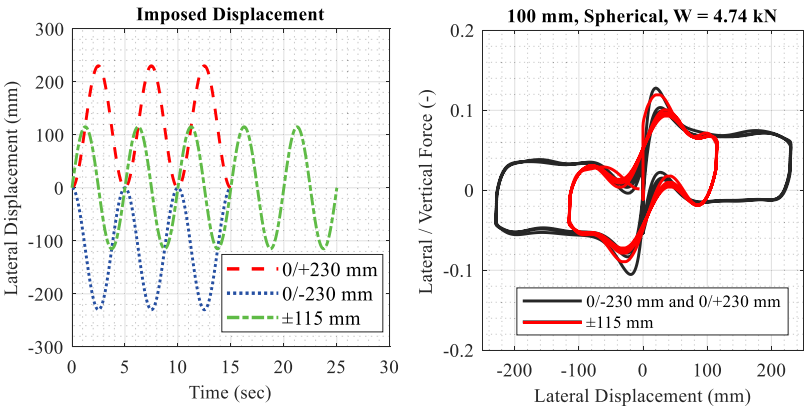

Figure 7. Left: displacement imposed by the shake table during the lateral cyclic tests; right: representative comparison of the response of the isolators during the "0/+230," "0/-230" and "±115 mm" tests.

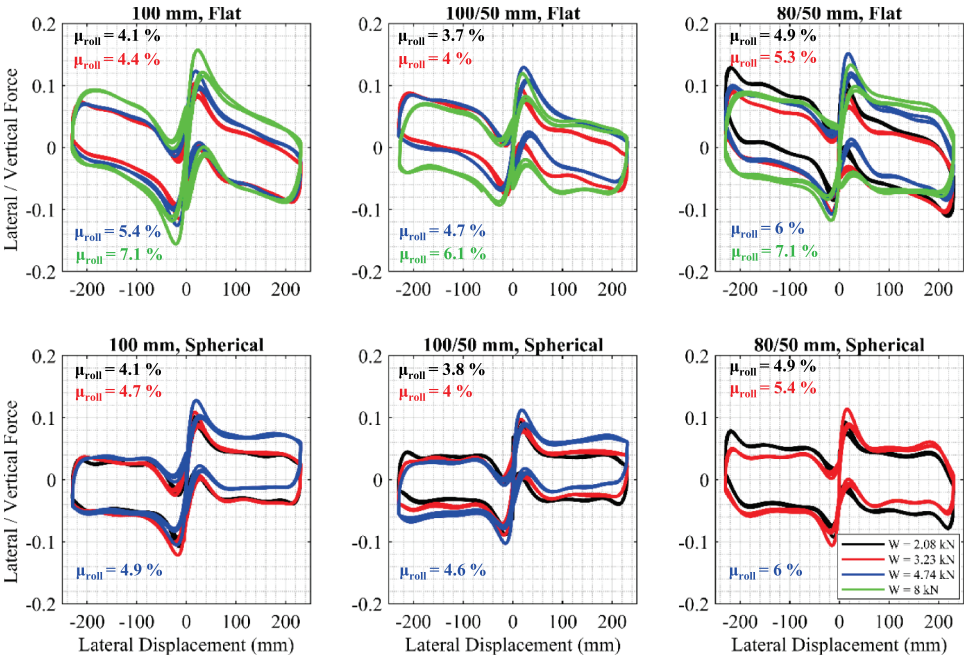

Figure 8. Influence of the vertical load (W) on the cyclic lateral response of the spherical isolator.
Note that, since μ_{roll} was obtained from the "±115 mm" loops while there were certain "±230 mm" tests that were not performed, in Fig. 8 there are cases where a μ_{roll} is offered, without the corresponding loop.

Fig. 8 collectively offers the force deformation loops for all the ±230 tests (that took place before the shake table tests). The first and most important observation is that the behavior of the system is clearly not bilinear elastoplastic (that is, it does not comprise an elastic and a perfectly plastic material model in parallel) as the rigid body model with friction would imply. Hence, attempting to approximate it as such should be avoided, at least for the loads, curvatures, and materials considered in this study. In fact, since the sphere has deformed to an oval-shaped object (which this paper will continue to name "sphere" for reasons of language simplicity), a vertical motion of the top plate was recorded. This vertical motion influences the restoring force. In energy terms, it influences the gravitational potential energy. This should result in a fluctuation of the restoring force with peaks every $\pi \times D$ of displacement. For the cases studied in this paper, this displacement corresponds to 314 mm and 251 mm for the spheres having $D =$ 100 mm and $D = 80$ mm, respectively. These displacements fall outside the applied displacement range, and such a periodic performance was not recorded.

The rolling friction coefficient, μ_{roll}, is conventionally defined as the lateral-to-vertical force ratio at zero lateral displacement and is an indicator of the energy dissipation capacity of the isolator. In all following sections, the rolling friction coefficient was obtained by the "±115 mm" cyclic tests and was defined as the ratio of the lateral-to-vertical force when crossing zero lateral displacement. This rolling friction coefficient, μ_{roll}, is also given in Fig. 8.

As defining μ_{roll} via the lateral force amplitude at zero lateral displacement puts a lot of emphasis on one part of the load-deformation curve, in particular an area that is heavily influenced by the flattening of the sphere, two alternative definitions are also explored:

a) $\mu_{roll,DE} = W_{DE}/(4 \times W \times u_o)$, where W_{DE} is the energy dissipated in one loop, W is the vertical force, and u_o the amplitude of the test (= 230 mm) and b) $\mu_{roll,100} = (F_{100}^{+} - F_{100}^{-})/W$ where F_{100}^{+} and F_{100}^{-} is the lateral load at 100 mm when loading and unloading, respectively. Fig. 9 shows that all 3 μ_{roll}, $\mu_{roll,DE}$, $\mu_{roll,100}$ are close to each other, with μ_{roll} being approximately 10% larger than $\mu_{roll,DE}$ or $\mu_{roll,100}$. This 10% difference is negligible in comparison to the velocity-

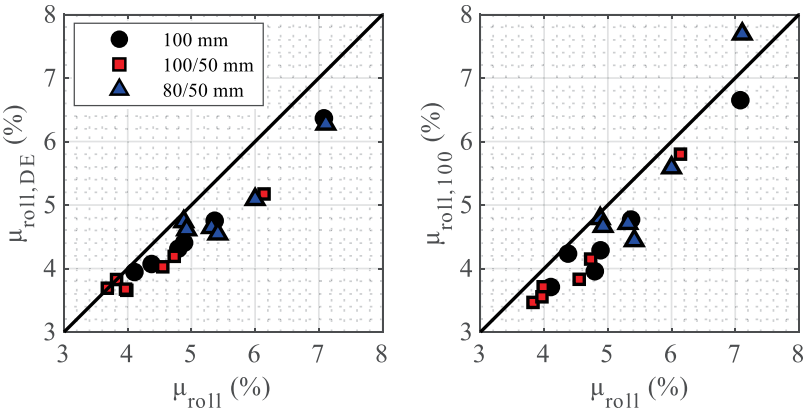

Figure 9. Comparison of different approaches for obtaining the rolling friction coefficient.

dependency of μ_{roll} (detailed explanation in section 8). Therefore, for the rest of this paper μ_{roll} will be used.

Overall, the lateral cyclic response of the spheres comprises the following branches:

(1) An initial ascending (positive stiffness) branch up to the maximum value of the lateral-to-vertical force ratio, which ranges between 0.093 and 0.156 and corresponds to a lateral displacement ranging between 15 mm and 30 mm (model scale). This value of lateral load and displacement depends on the type of isolator and the vertical load level, with more compressed spheres tending to have slightly larger values. It is related to the compressive and creep displacement and, hence, the shape change of the isolator. In fact, this behavior is related to the rolling of the sphere up-and-over the depression that was caused by the gravity load (noted as "Flat surface" of the deformed sphere in Figure 2, Right).
(2) After the peak lateral force is reached, the isolators exhibit negative stiffness (negative slope of the force displacement curve) for lateral displacements larger than 30 mm (model scale). In all tested cases, this negative stiffness branch reached lateral displacements at the order of 70-80 mm. This negative stiffness is related to the deformed shape of the isolator.
(3) At these lateral displacements (larger than 70 mm), the influence of the curvature of the concrete plate (flat or spherical) becomes pronounced. For the isolators with flat concrete plates, the stiffness remains negative for the whole range of tested displacements. For isolators with spherical concrete plates and lateral displacements larger than 80 mm, the stiffness of the isolator becomes practically zero since the positive stiffness induced by the concrete plates cancels the negative stiffness induced by the deformed sphere. For the configuration with 100/50 spheres, spherical plates, and $W = 4.74$ kN, a mildly positive stiffness was observed (10^{-4} (-)/mm), as seen in Fig. 8.
(4) After a full sinusoidal motion is completed, the subsequent cyclic loops closely follow the path of the first. The peak load of the second circle is approximately 20% lower than the peak load of the first. It cannot be concluded whether this is a consequence of the Mullins effect (Diani, Fayolle, and Gilormini 2009; Mullins 1969) or of the initial deformation of the sphere due to creep. This limited strength degradation is only observed at the peak load and only between the first and the second circle. After that, the response remains stable.
(5) In all tests, the thickness of the loops (i.e. the vertical distance between the loading and unloading part) is practically constant for the whole range of tested displacements, with the exception of zero lateral displacement, since the "±230 mm" is composed of two different tests. This shows constant energy dissipation that is not related to the amplitude of the lateral displacement but is mainly associated with μ_{roll}.

It should be noted that the above observations regarding the non-bilinear response of the isolators are limited to the specific curvatures studied. Intuition, as well as the tests on mortar-filled tennis balls (Katsamakas et al. 2021b), suggest that as the thickness of the rubber layer tends to zero, the behavior of the system will tend to a bilinear system with a lower coefficient of rolling friction.

6.1. Influence of the Vertical Load (Weight) and the Curvature of the Concrete Plates

From Fig. 8 it can be deduced that the coefficient of rolling friction (μ_{roll}) increases with compression. The influence of the vertical load (i.e. weight of the supported superstructure) is moderate, with an increasing vertical load leading to a mildly higher rolling friction coefficient (μ_{roll}) and higher energy dissipation.

Fig. 10 offers an indicative comparison of flat and spherical isolators. For small displacements (smaller than 70 mm), the curvature of the concrete surface does not influence the response. However, for larger displacements, where the flat case exhibits negative stiffness, the positive stiffness induced by the concrete curvature keeps the overall tangent stiffness around zero. The conclusions drawn regarding the influence of the spherical plates are linked to the specific set of parameters (curvature of concrete plates, stiffness of rolling isolator, supported weight, magnitude of lateral displacement). Using spherical plates with a lower radius of curvature (R) would lead to an even more pronounced effect of the curvature. As expected, the curvature of the isolator does not influence the rolling friction coefficient.

6.2. Influence of the Steel Core and of the Thickness of the Rubber Shell

Fig. 8 shows that the presence of a 50 mm steel core inside a sphere with an external diameter of 100 mm leads to lower values of rolling friction coefficient (10–20% lower) and, thus, decreased energy dissipation, without affecting the shape of the lateral cyclic response. These differences are negligible under low compressive load (e.g. 2.08 kN/sphere) but become more pronounced under high compression (e.g. 8 kN/sphere).

Fig. 8 also shows the influence of the thickness of the rubber shell around the 50 mm steel core by comparing the 80/50 mm to the 100/50 mm spheres. The influence of this parameter is limited for all the configurations considered herein, with the rolling friction coefficient ranging between (3.7% and 6.1%) and (4.9% and 7.1%) for the 100/50 and the 80/50 spheres, respectively. Therefore, the 100/50 and the 80/50 spheres have a very similar lateral cyclic response with the only difference being the μ_{roll} values that are 15–25% higher when 80/50 spheres are used. Overall, there is a clear trend that is discussed more extensively in section 6.4: μ_{roll} increases with δ/D no matter the size of the sphere and the presence of a steel core.

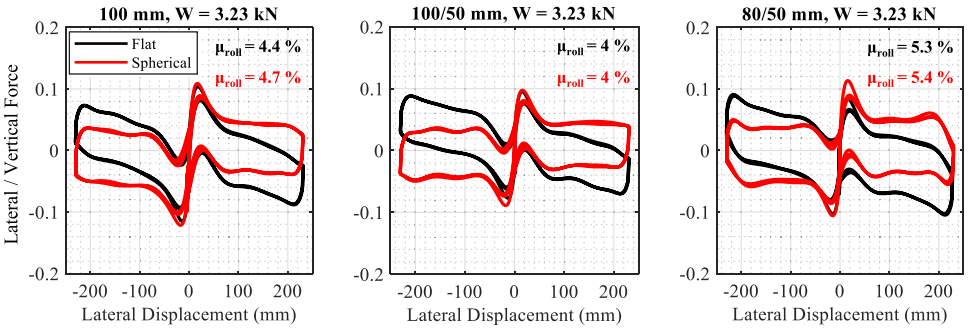

Figure 10. Influence of the curvature of the concrete plates, for all tested spheres, under W = 3.23 kN of compressive force.

6.3. Influence of Grease (Surface Lubrication)

After performing the cyclic tests, the spheres and the concrete surfaces were covered with grease to reduce interface friction between the rolling sphere and the concrete substrate. No measurements of the interfacial friction were performed, but it is reasonable to assume that grease reduced it. Reducing the interfacial friction coefficient would allow for a) understanding whether part of the energy dissipation originates from interfacial sliding between the rolling sphere and the concrete plates and subsequently b) whether the rolling friction coefficient (μ_{roll}) is affected by the sliding friction of the aforementioned interfaces. It was proved that neither energy dissipation nor μ_{roll} depend on the sliding friction of the sphere-concrete interface since the cyclic plots, with or without the use of grease, are practically identical (Fig. 11). This implies that, for the rolling spheres tested in the present study, the largest part of energy dissipation originates from the continuous deformation (shape change) of the rolling sphere, which is made of an energy-dissipating material. These findings are in agreement with the experimental results of Tabor (1955) and Eldredge and Tabor (1955), who tested steel spheres rolling on softer metals to understand the nature of rolling friction.

6.4. Relation Between Compressive Deformation and Rolling Friction Coefficient

Based on tests of solid balls made of 85A Natural Rubber (NR) balls, Katsamakas et al. (2022) argued that an approximate relation between compressive deformation and rolling friction coefficient exists. Fig. 12 (left) offers a comparison between the experimental results of the tests discussed in this paper,

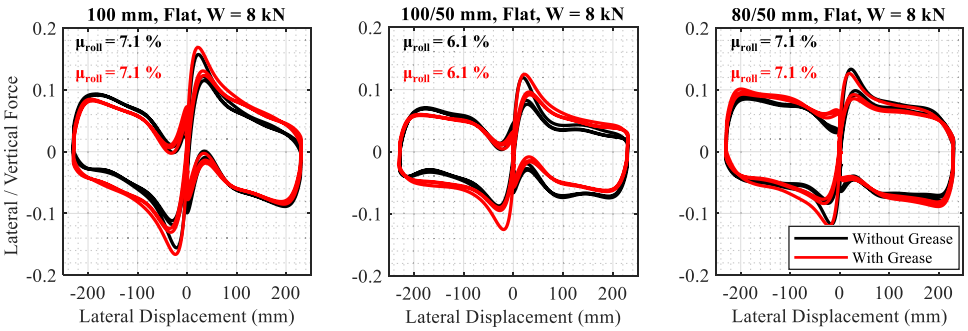

Figure 11. Influence of the interfacial friction coefficient on the cyclic loops.

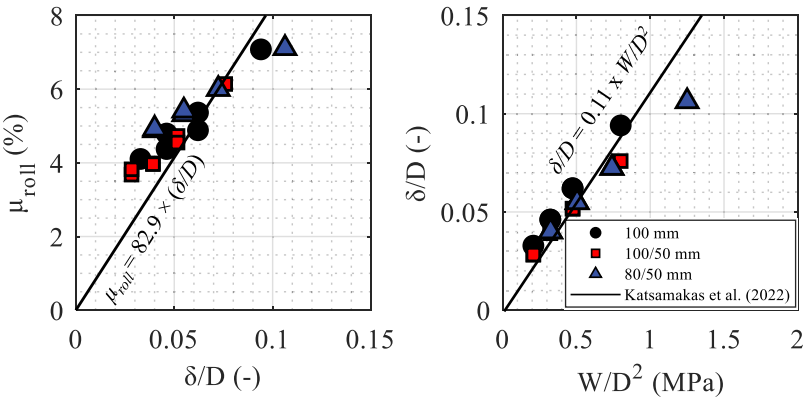

Figure 12. Correlation of the rolling friction coefficient (μ_{roll}) with the non-dimensional compressive displacement (δ/D), and the characteristic stress (W/D^2).

compared to the analytical expression proposed in (Katsamakas et al. 2022) that was derived for softer (Shore 85A) solid PU spheres of 100 mm diameter.

The comparison shows that the expression performs relatively well, even though it was derived for spheres of different hardness. Fig. 12 (right), shows a linear dependence between the non-dimensional compressive displacement (δ/D) and the characteristic stress (W/D^2). Note that this linearity cannot be extrapolated, as Fig. 6 shows a clear hardening for larger loads.

7. Shake Table Tests

7.1. Indicative Results

Fig. 13 plots the top slab ("Superstructure") acceleration – displacement loops of the isolated slab for the 345 component of the Lucerne near-field pulse-like record from the 1992 Landers (USA) earthquake. This ground motion was not acceleration-scaled. The PGA, PGV, and PGD of the motion were 0.79 g, 200 mm/sec, and 127.7 mm. The results show that the acceleration transmitted to the superstructure is mildly influenced by the vertical load or type of sphere, with lower vertical loads leading to slightly lower accelerations. The dependence on vertical load is clearly larger for the solid 100 mm sphere, because it is more flexible. The influence of the curvature of the concrete plate is moderate, leading to larger accelerations and lower displacements for the spherical isolators. For example, for the case of $W = 2.08$ kN and 100/50 mm, when spherical plates were used, the accelerations increased from 0.121 g to 0.148 g, whereas the displacements decreased from 36.1 mm to 25.1 mm. It is noted that the specific ground motion led to lateral displacements below 50 mm (model scale); for larger lateral displacements, the effect of the curvature of the concrete plates becomes more pronounced (section 6.1). Notably, the shake-table tests were repeatable: Several ground motions were run 3 times, and the response was practically identical, both in terms of displacements and accelerations.

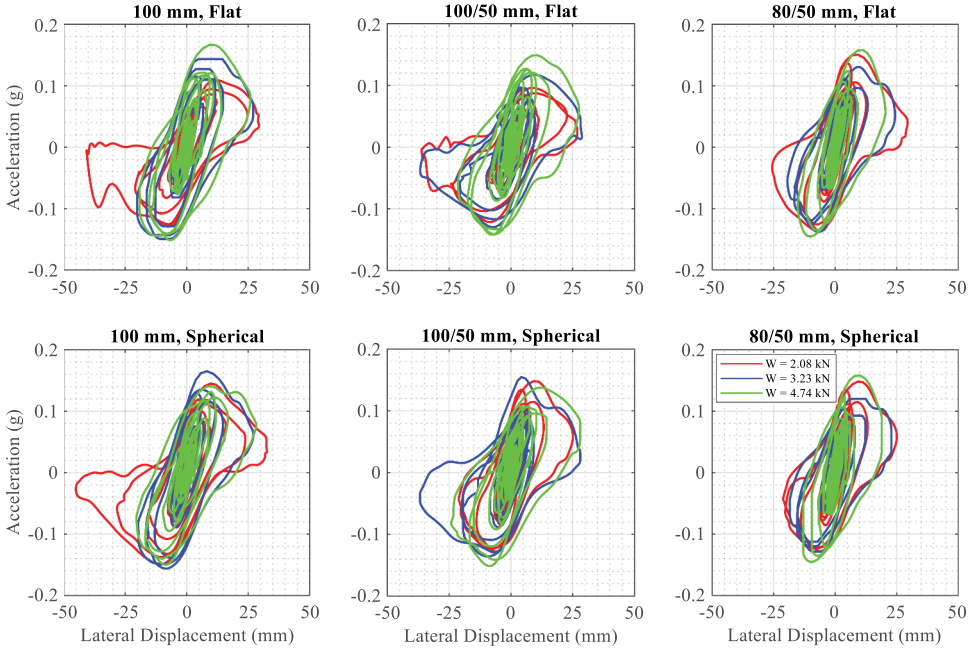

Figure 13. Dynamic response of the isolation system in terms of displacements-accelerations, as obtained during the 345 component of the 1992 Landers (USA) ground motion, as recorded at Lucerne station.

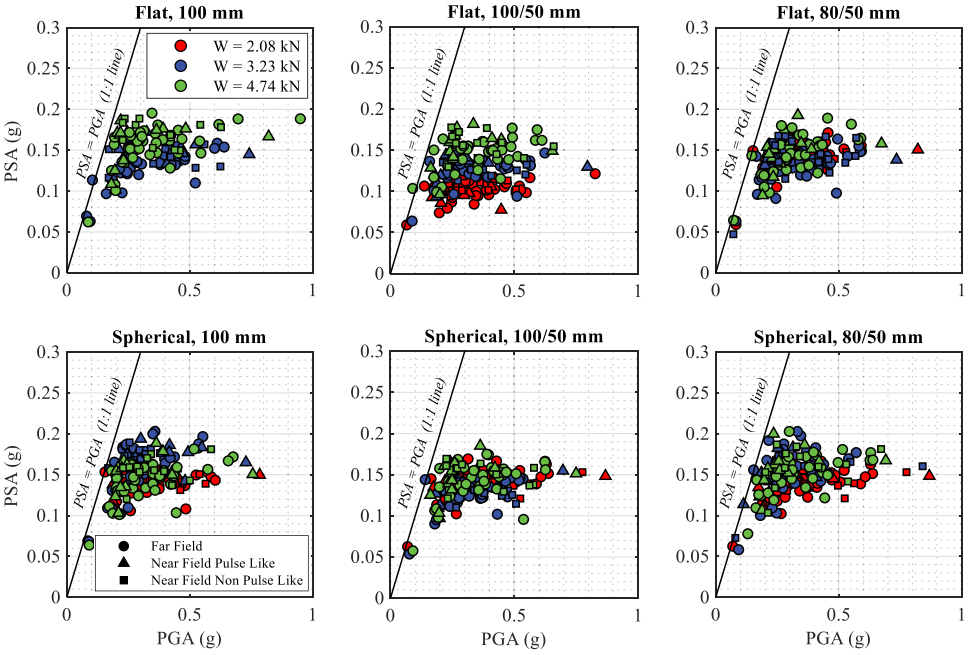

Figure 14. Correlation between the acceleration transmitted to the superstructure (PSA) and PGA for all tested configurations. Top, flat concrete plates; bottom, spherical concrete plates.

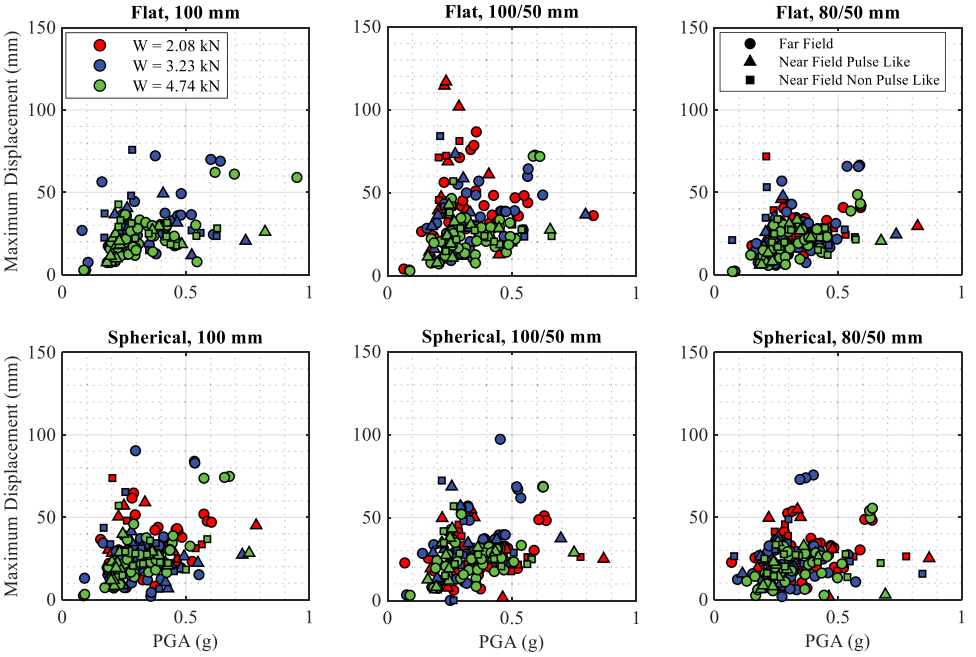

Figure 15. Correlation between the maximum displacement of the isolators and PGA for all tested configurations. Top, Flat concrete plates; Bottom, Spherical concrete plates.

7.2. Scatter Plots for All Ground Motions

Figs. 14–16 show scatter plots between PGA and a) The acceleration of the top slab (Peak Superstructure Acceleration – PSA), b) the peak displacement of the isolators, and c) the residual displacement of the isolators. The far-field ground motions, the near-field pulse-like motions, and the near-field non-pulse-like ground motions are noted with circular, triangular, and square marks, respectively. The acceleration measurements of the configuration with flat concrete plates, 100 mm spheres, and $W = 2.08$ kN are not shown in the following plots since, due to a data acquisition problem, the accelerations of this configuration were not measured.

For excitations with relatively small PGAs (smaller than 0.10–0.15 g – depending on the configuration) that are not strong enough to start rolling the system, the superstructure acceleration is roughly equal to the PGA. However, for larger PGAs, the superstructure acceleration seems capped by values that are slightly higher than the peak of the force deformation loops of the cyclic loops. For all configurations and ground motions, PSA does not exceed 0.20 g. The isolator maintained moderate peak displacements during ground motion shaking, which were below 120 mm and 100 mm for the flat and the spherical plates, respectively (i.e. 240 mm and 200 mm in the prototype scale).

In all configurations with spherical plates, the residual displacement was negligible (lower than 2.7 mm). The same conclusion holds for the flat plates, with the exception of 2 configurations where residual displacements of 68 mm and 70 mm were observed. For these two tests, the maximum displacements were 81 mm and 102 mm, respectively (model scale). These two tests used as excitations the 282 component of the Imperial Valley-06, USA ground motion as recorded at the Chihuahua station (PGA = 0.23 g, PGV = 190 mm/sec, PGD = 33.7 mm) and the 0 component of the Kobe, Japan ground motion as recorded at the Shin-Osaka station (PGA = 0.20 g, PGV = 200 mm/sec, PGD = 37.7 mm). Notably, these two tests were not the ones with the larger PGA, and no systematic trend between the residual displacement, the maximum displacement, and the PGA is observed. These two ground motions are mainly characterized by their high PGV; hence, even though no clear trend between the displacement of the isolator and the PGV is observed, this could be a starting point for further

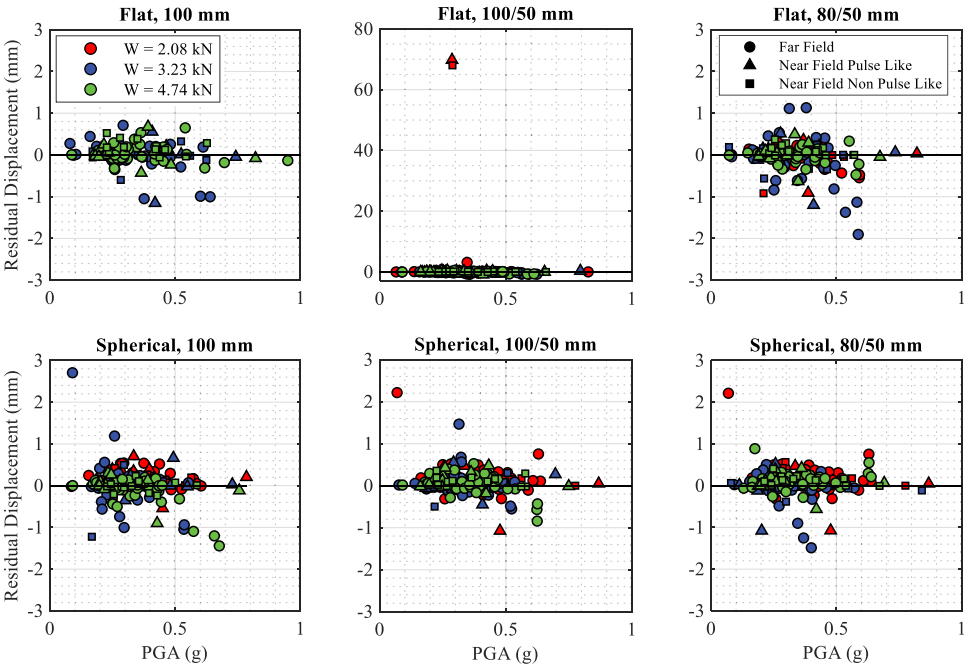

Figure 16. Correlation between the residual displacement of the isolators and PGA for all tested configurations. Top, Flat concrete plates; Bottom, Spherical concrete plates.

research. It is noted that, after the conclusion of each shake-table test, if the residual displacement exceeded 1 mm, the isolators were placed back to zero position before the initiation of the next shake-table test.

Overall, for the vast majority of the ground motions considered, the residual displacement was negligible, even when flat isolators were used. This conclusion is linked to the applied uniaxial seismic excitation. A three-dimensional excitation would lead to different isolator displacements. Given the current state of the practice in low-income countries, one could consider using flat isolators in cases where manufacturing the spherical molds is not technically feasible. However, more research is needed in this direction to take into account the influence of any accidental inclination on systems exhibiting these novel loops that significantly deviate from a pure friction model for which a restoring force is necessary (Constantinou, Mokha, and Reinhorn 1991; Tsopelas and Constantinou 1997).

After the shake table tests, a set of cyclic tests was performed again to evaluate the deterioration of the spheres. The response was practically the same. Hence, no deterioration occurred.

8. Phenomenological Modeling of the Isolators

This section presents a 5-parameter phenomenological numerical model that is used to model the uniaxial lateral dynamic behavior of SDRSIs. The model can be easily extended to model the planar lateral behavior. Such an analytical prediction of the response is fundamental in the design of a seismic isolation system, in developing simplified methods of analysis, and in performance evaluation. Three different isolation configurations are examined as representative of the experimental results, using different types of spheres (100 mm, 100/50 mm, or 80/50 mm), concrete plates curvature (flat or spherical), and vertical load levels (3.23 kN or 4.74 kN).

8.1. Calibration Based on the Lateral Cyclic Tests

The phenomenological model is described by the following equation (Equation 3):

$$F/m = (\omega^2 \times u) - (Q \times sign(\dot{u})) + (Q_2 \times \tanh(10 \times u)) - (Q_3 \times u) + (a_1 \times sign(u) \times betapdf(|u/a_2|)) \quad (3)$$

where F is the restoring force of the isolator, m is the mass that the isolator carries, u is the horizontal displacement of the isolator, and ω is the cyclic frequency of rolling motion on the spherical plates according to the rigid body model. For the spherical plates used in the present study, $\omega = 1.83$ rad/s (Table 2). The cyclic frequency of rolling motion is equal to zero when flat plates are used. The force at zero displacement (normalized to m), Q, is equal to $\mu_{roll} \times g$, where μ_{roll} is the rolling friction coefficient (measured from the force at zero displacement) and g is the gravity acceleration. The term Q_2 is a parameter of the phenomenological model that controls the additional breakaway force sourcing from the flattening of the sphere. The term Q_3 controls the negative stiffness branch that sources from the flattening (shape-change due to compression and creep) of the sphere. The units of all the parameters used in the model are: u (m), Q (m/s^2), Q_2 (m/s^2), Q_3 (1/s^2), α_1 (m/s^2), α_2 (m). The numerical model assumes rigid behavior for the superstructure. The "ode45" solver of MATLAB (Mathworks, 2022; Shampine and Reichelt 1997) was used to solve Eq. (3). This single-step solver is typically used to solve nonstiff differential equations and is based on an explicit Runge-Kutta formula, the Dormand-Prince pair (Dormand and Prince 1980). The solver is defined by two parameters; the relative and the absolute error tolerance. These parameters were set to 10^{-3} mm and 10^{-6} mm. Preliminary parametric analyses revealed that further refinement of these parameters does not increase the accuracy of the model, but only result in longer solution time.

The probability density function of the beta distribution is noted as *betapdf* (Wasserman 2004). The beta distribution is characterized by the factors α and β that define the shape of the curve. In the present model, $\alpha = 2$ and $\beta = 5$, to obtain a shape of the probability density function that is compatible

to the experimental tests (these values of α and β remained unaltered in all cases). The parameters a_1 and a_2 modify the height and the lateral displacement of the distribution, and are calibrated based on the experimental results. Note that the model applies only for rotations of the balls smaller or equal to the ones that this paper has tested. It cannot be used to extrapolate to larger rotations.

Firstly, the Q_2, Q_3, a_1, and a_2 parameters are manually calibrated, through a trial and error procedure, with the aim of obtaining a good fit on the cyclic tests. Since the three studied isolation configurations were calibrated independently, the resulting values of Q_2, Q_3, a_1, and a_2 were different for each configuration (yet close to each other). The value of μ_{roll} was set as equal to the experimental force at zero displacement (noted in Fig. 8). Fig. 17 shows the results of this calibration procedure, together with the values of the parameters μ_{roll}, Q_2, Q_3, a_1, and a_2 that were used. The proposed model can capture the different parts of the response with reasonable accuracy. The model was calibrated on the behavior of the isolators *after* the first cycle – hence it does not capture the decrease of the breakaway force that is observed between the first and the second cycle. The values adopted for the parameters of the model (μ_{roll}, Q_2, Q_3, a_1, and a_2) depend on the sphere characteristics and the vertical load level.

8.2. Prediction of the Shake-Table Results

After the calibration based on the cyclic tests, the model was used to predict the shake-table response of the isolators. The response of the isolators is velocity-dependent. This can be deduced from Fig. 13, where (e.g. for the flat plates) the PSA is larger than the maximum lateral-to-vertical force ratio obtained from the lateral cyclic tests (Fig. 8). This is attributed to the rate-dependent mechanical properties of PU (Somarathna et al. 2020; Weißenborn, Ebert, and Gude 2016). It is assumed that this dependency originates primarily from μ_{roll}, with larger velocities leading to larger values of μ_{roll}. Due to the absence of lateral cyclic tests under larger velocities, a μ_{roll} – velocity relation was deduced from the shake table tests: At zero lateral displacements, the velocity of the slab was derived by differentiating its position. The acceleration of the system was directly measured at zero displacement. Dividing the acceleration with the gravity acceleration (g), provides μ_{roll}. Fig. 18 plots the values of μ_{roll} obtained for different velocities for some indicative cases. As the form of the experimental data is similar to the form of the friction coefficient – velocity relation for Teflon sliding bearings, an equation similar to the one proposed by Constantinou, Mokha, and Reinhorn (1990) is fitted to the data:

$$\mu_{roll} = f_{\max} - D_f \times \exp(-A \times |\dot{u}|) \tag{4}$$

where f_{max} is the value of μ_{roll} at large velocities, f_{min} is the minimum possible value of μ_{roll}, $D_f = f_{max} - f_{min}$, and A is a model parameter that controls the shape of the μ_{roll}-velocity curve. All these parameters are non-dimensional, with the exception of A, which is defined in sec/mm. The model was calibrated independently for each of the examined cases, and the resulting set of parameters is offered in Fig. 18.

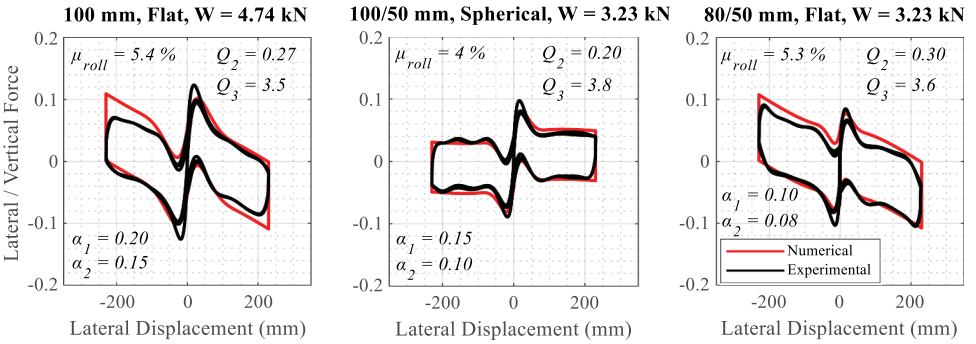

Figure 17. Calibration of the phenomenological model based on the lateral cyclic tests.

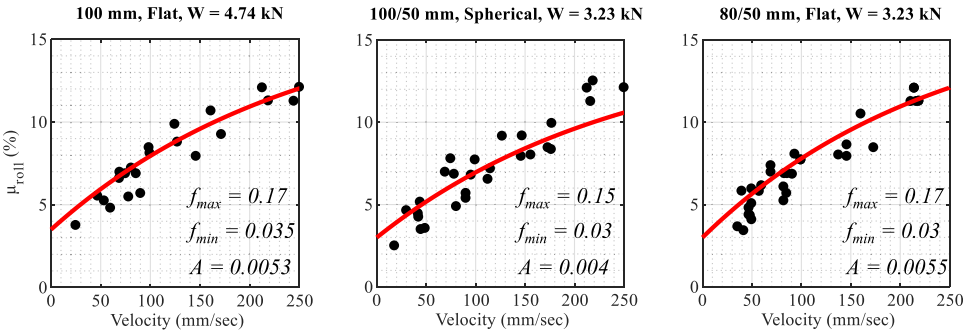

Figure 18. Calibration of the velocity-dependent value of the rolling friction coefficient (μ_{roll}).

The efficiency of the proposed model is assessed by comparing the shake-table and the numerical results. The values of the Q_2, Q_3, a_1, and a_2 parameters used in each configuration for the prediction of the shake-table tests are equal to the ones used in the lateral cyclic tests (noted in Fig. 17). The corresponding values of the velocity-dependent μ_{roll} appear in Fig. 18, which is the only parameter that differs between the lateral cyclic and the shake-table tests. The response parameters of interest are the maximum displacement (u_{max}) and the Peak Superstructure Acceleration (PSA). Two different comparison approaches are employed; a one-by-one comparison and a statistical model validation approach (Bachmann et al. 2018; Yim, Chopra, and Penzien 1980).

8.2.1. One-By-One Comparison

Figs. 19 and 20 compare the results of the phenomenological model to the experimental ones for two specific ground motions; the 345 component of the 1992 Landers (USA) ground motion, as recorded at Lucerne station and the 0 component of the 1989 Loma Prieta (USA) ground motion, as recorded at Capitola station, respectively. These ground motions were selected as they were strong enough to induce moderate-to-large displacements to the isolators.

The phenomenological model approximates the experimental acceleration-displacement response with satisfying accuracy, including both the positive and the negative stiffness branches (Figs. 19, 20, first row). The absolute maximum experimental displacement is similar to the phenomenological one, and the corresponding time-history is adequately captured; however, there are non-negligible displacement spikes that are not captured by the phenomenological model (Figs. 19, 20, second row). The acceleration time-history of the phenomenological model is similar to the experimental one, and predicts the maximum acceleration with high accuracy (Figs. 19, 20, third row). The accelerations predicted by the phenomenological model have a higher frequency content that is particularly evident in the beginning and at the end of the excitation, when the corresponding lateral displacements are low. This is also evident in the limited decay of the acceleration time history (Fig. 20). This deviation is clear in the acceleration response spectra, where the phenomenological response produces consistently higher values of Sa (g) and non-negligible spikes at higher frequencies (Figs. 19, 20, fourth row). Fig. 21 shows the absolute error of the predictions of u_{max} (top row) and PSA (bottom row). The maximum absolute error in predicting PSA is approximately 32%, while in most cases it is below 10%. The error in predicting u_{max} is much larger: The model can overpredict up to 160%. However, this large value of error is related to very small displacements that would not govern design. For ground motions that induced more than 20 mm displacement (40 mm in the prototype scale), the absolute error of u_{max} predictions is smaller than 50%, and in most cases, smaller than 25%. The general trend observed is that, as the displacements increase, the error reduces. Therefore, the model predicts accurately the strong excitations that are critical for design. Fig. 21 also shows the average absolute error for each configuration and response magnitude.

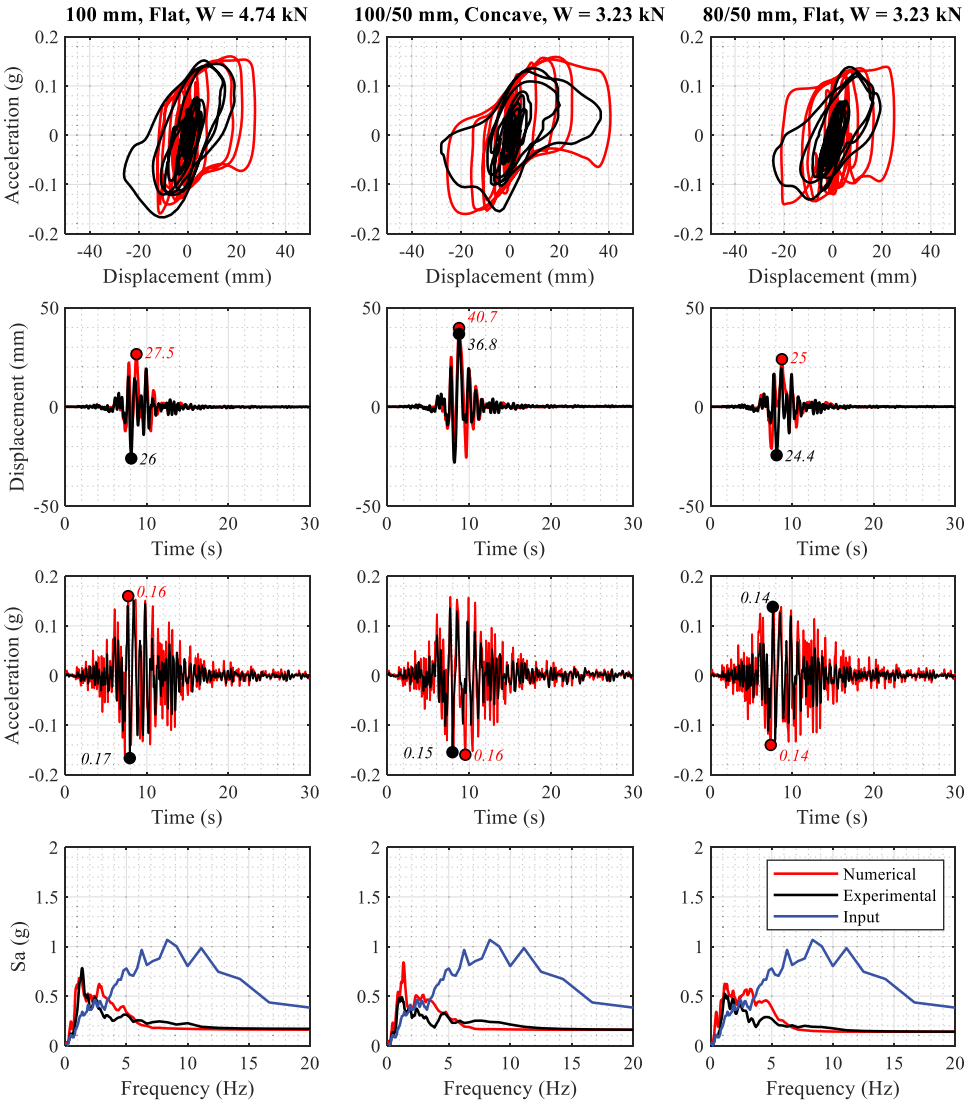

Figure 19. Comparison of the experimental and the numerical response of the studied configurations during the 345 component of the 1992 Landers (USA) ground motion, as recorded at Lucerne station (near-field pulse-like ground motion).

Among the 3 isolators discussed in this section, the highest average absolute error is 28.1% and 7.4% for u_{max} and PSA, respectively. Moreover, the phenomenological model does not consistently under- or overpredict the response.

Fig. 22 compares the experimental and the numerical results, both for the maximum displacement (u_{max}) and the PSA, using a scatter plot. The vast majority of the points is concentrated close to the diagonal (with the line showing equality between the two axes), meaning that the experimental and the numerical results are closely correlated. Moreover, the scatter (distance from the diagonal) is reduced as the values of u_{max} increase, indicating that the model is more accurate at larger lateral displacements. These large lateral displacements are the ones that govern design. The accuracy of the model is also confirmed by the correlation coefficient (R) that ranges between 0.77 and 0.91, indicating strong correlation (Fig. 22).

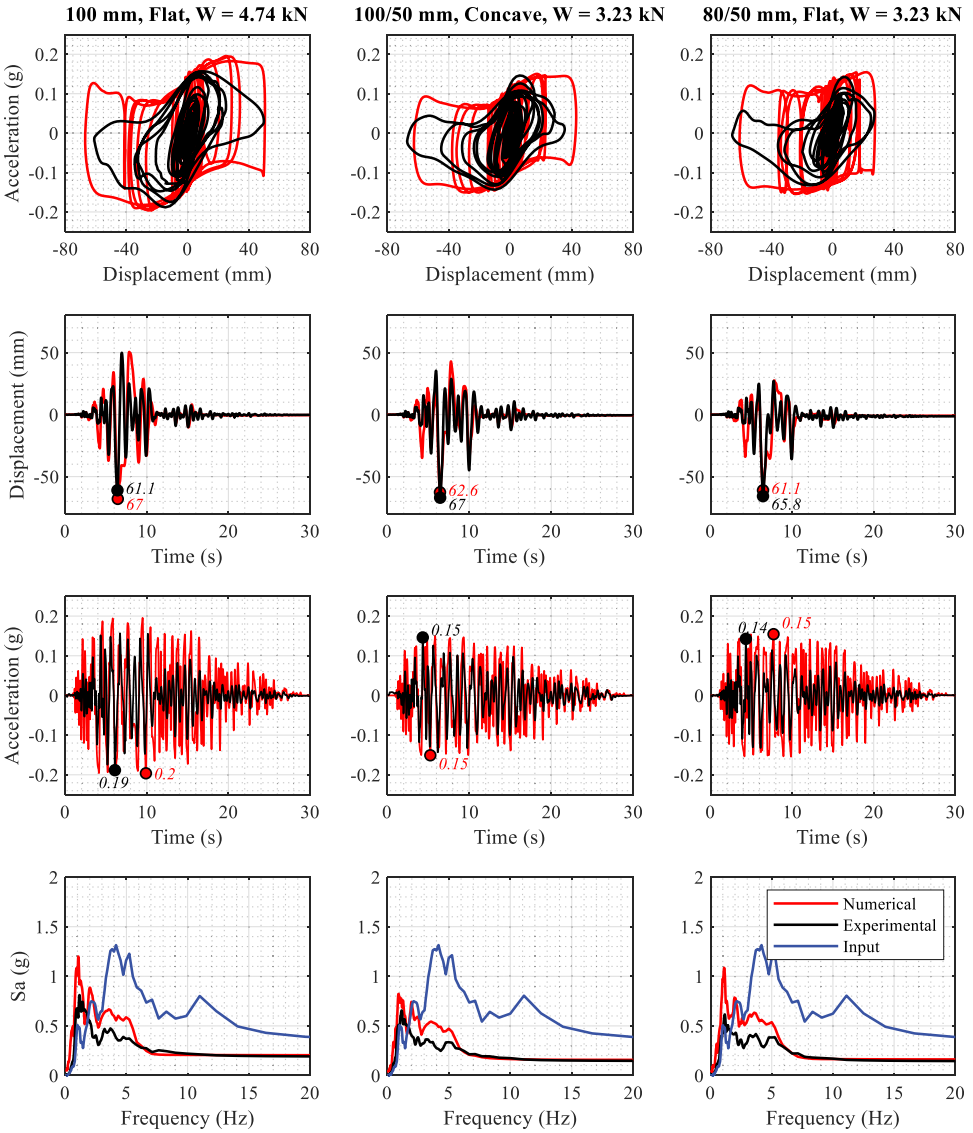

Figure 20. Comparison of the experimental and the numerical response of the studied configurations during the 0 component of the 1989 Loma Prieta (USA) ground motion, as recorded at Capitola station (far-field ground motion).

Overall, the observed accuracy of these predictions is also consistent with the results obtained by Ipek, Wolff, and Constantinou (2021) for structures with different seismic isolation systems. It is noted that, for real buildings and more complex, three-dimensional seismic excitation, the error of the analytical prediction is expected to increase. The error of the analyses presented both in this paper and in the study of Ipek, Wolff, and Constantinou (2021) is the result of uncertainties in the behavior of the tested structures, which can be accounted for in analysis and design using bounding methods of analysis.

8.2.2. Statistical Comparison

The statistical model validation approach compares the Cumulative Distribution Functions (CDFs) of the main response quantities of the experimental results and the phenomenological model. The accuracy is quantified using the *p*-value of the two-sample Kolmogorov-Smirnov test (statistical comparison) (Kolmogorov 1933; Smirnoff 1939). In the Kolmogorov-Smirnov test, two hypotheses,

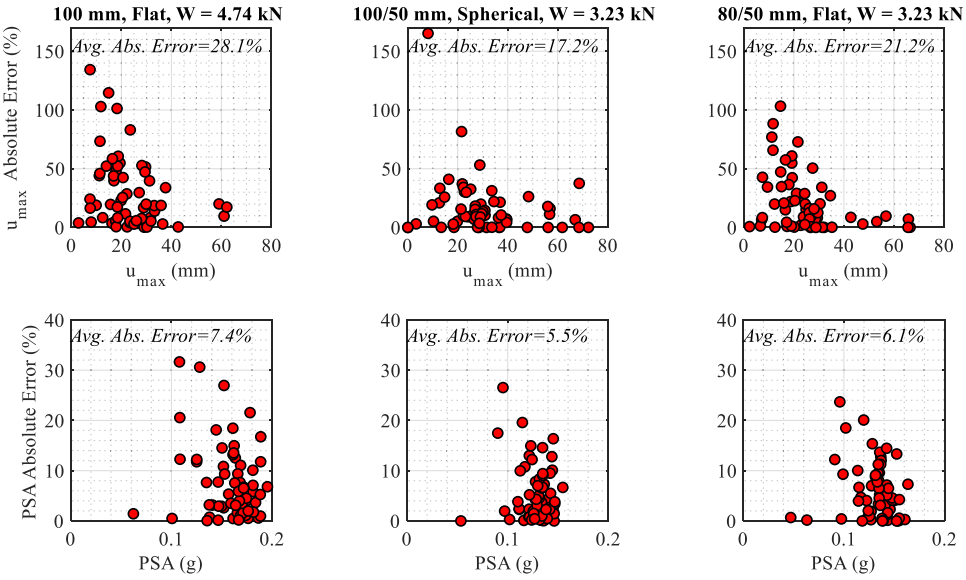

Figure 21. Absolute error of the phenomenological model in comparison to the experimental shake-table tests.

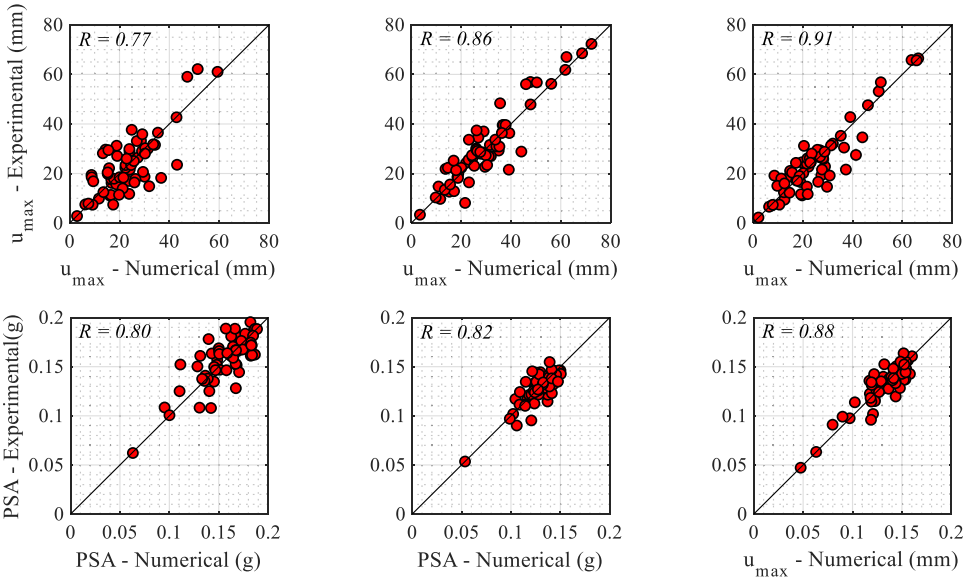

Figure 22. One-by-one comparison of the results of the phenomenological model to the experimental shake-table tests.

H_0 (which is tested), and its opposite, H_1, are considered. The tested null hypothesis H_0 is rejected when the p-value of the K-S hypothesis test is lower than a statistical significance threshold, which is typically set to 0.1 (Wasserman 2004). The p-value is the outcome of the test and does not indicate the probability that H_0 is true, but rather the probability that, if hypothesis H_0 is true, the observed outcomes would conform with the opposite hypothesis H_1. A detailed explanation of hypothesis testing procedures can be found in (Kolmogorov 1933; Smirnoff 1939; Wasserman 2004). In our case, the null hypothesis (H_0) is that the experimental and the numerical CDFs for u_{max} and PSA converge to the same, yet unknown, CDF. The p-value was computed for the following hypotheses:

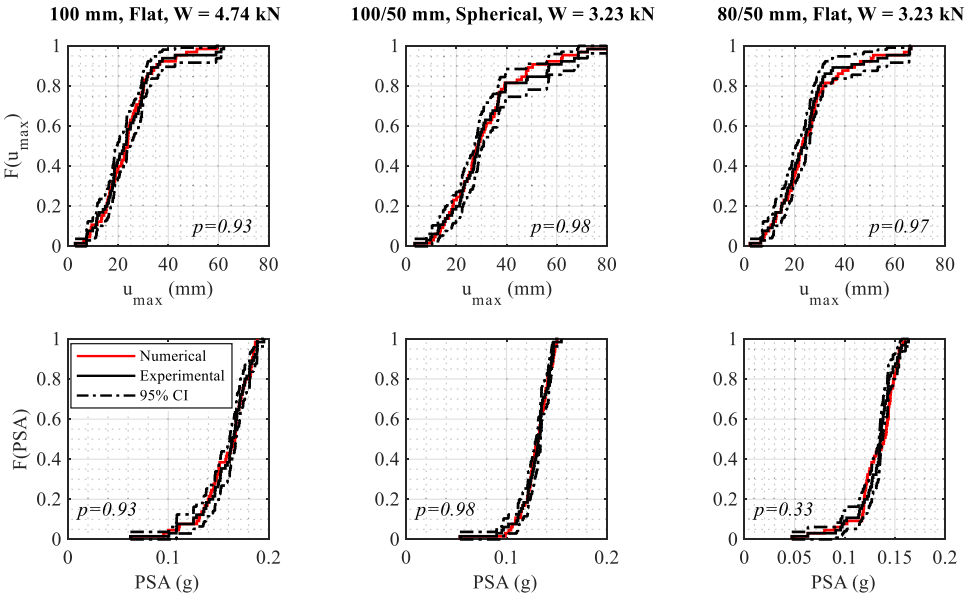

Figure 23. Statistical comparison of the results of the phenomenological model to the experimental shake-table tests.

$$H0 : \bar{F}_{Numerical} = \bar{F}_{Experimental} \text{ vs } H1 : \bar{F}_{Numerical} \neq \bar{F}_{Experimental} \tag{5}$$

where $\bar{F}_{Numerical}$ and $\bar{F}_{Experimental}$ are the numerically and experimentally estimated CDFs. Fig. 23 compares the numerical and experimental CDFs of u_{max} (top row) and PSA (bottom row). The CDFs match well. In fact, the CDF calculated using the phenomenological model is always within the 95% Confidence Interval (CI) of the experimental response both for u_{max} and PSA.

The calculated values of the two-sample Kolmogorov-Smirnov test (p-values) range between 0.93 and 0.98 for u_{max} and between 0.33 and 0.98 for the PSA (Fig. 23). Therefore, for all cases, the p-value is at least 0.33, which is well above the 0.1 threshold, that is typically used for two-sample testing (Wasserman 2004). Hence, the experimental and the numerical results originate from the same CDF.

9. Summary, Conclusions, and Future Research

The present study investigated the compressive, creep, lateral cyclic, and shake-table response of an isolator based on rolling PU spheres of shore hardness 95A (with and without steel core) rolling on concrete plates. Different levels of supported weight and curvatures of concrete plates were considered. A total of 21 different combinations of vertical load, sphere dimensions, and concrete plate curvature were tested under lateral cyclic loading. In the shake-table tests, 18 combinations were tested with 65 ground motions each, leading to a total of 1170 shake table tests. Subsequently, a phenomenological model was calibrated based on the lateral cyclic tests and was used to predict the shake-table response of the proposed isolators. According to the experimental and the numerical results, the following conclusions are drawn:

(1) The compressive strength of the spheres is substantially higher than the estimated design vertical load applied to the spheres, considering an application in a low-rise residential masonry structure in low-income countries. The presence of the steel core makes the isolators stiffer.

(2) The lateral cyclic response differs substantially from the one that a rigid body model would suggest. This is due to the non-negligible deformability of the spheres that leads to both positive and negative stiffness branches. Change in gravitational potential energy and, therefore, restoring force occurs not only because of the curvature of the concrete surface but also because of the oval shape to which the spheres deform.
(3) The lateral cyclic response is affected by the curvature of the concrete surface. When spherical plates are used, the stiffness of the system increases. The final stiffness of the isolators is affected by the deformed shape of the isolators (source of negative stiffness) and the curvature of the concrete plate (source of positive stiffness). For the curvature of concrete plates, spheres and loads considered, the influence of the curvature of the concrete plates is particularly evident in large lateral displacements (larger than 70 mm in model scale), where the stiffness may reach either zero or mildly positive values.
(4) An increase in the vertical load (W) leads to a linear increase of the rolling friction coefficient (μ_{roll}). In fact, for the part of the parameter space considered, the rolling friction coefficient is practically linearly related to the non-dimensional compressive displacement (δ/D) and the characteristic stress (W/D^2). The rolling friction and energy dissipation source from energy dissipation within the sphere – not from surface friction with the concrete plates. Therefore, different compounds could exhibit different rolling friction.
(5) During the uniaxial shake-table tests with excitations at the order of the seismicity of Santiago, Cuba, the isolators significantly reduced the accelerations transmitted to the superstructure (in the range of 0.15 g), while maintaining displacements below 120 mm in the model scale (240 mm in the prototype scale). In all tests with spherical plates, the residual displacement was practically zero (i.e. less than 2.7 mm). Even when flat plates were used, the residual displacement was less than 4 mm with the exception of 2 tests. These values hold under the applied uniaxial seismic excitation and neglect the superstructure flexibility. The presence of bi-directional horizontal motion would influence the results. The vertical ground motion component is also expected to influence the response of the proposed gravity-based isolators. In a practical application, the use of one concave plate is suggested to reduce residual displacements.
(6) When the same isolators were subjected to 3 identical sequential uniaxial shake table excitations, the measured response, both in terms of accelerations and displacements, was practically the same. Therefore, the performed shake-table tests were repeatable.
(7) Even after being subjected to 65 uniaxial ground motion excitations, the isolators do not deteriorate, and their cyclic lateral response remains practically unaffected by the loading history.
(8) A 5-parameter phenomenological model was developed and calibrated based on the lateral cyclic tests. The proposed model accurately captured both the positive and the negative stiffness branches of the lateral cyclic response and accurately accounts for large lateral displacements.
(9) A velocity-dependent law for μ_{roll} was introduced to the phenomenological model, that was used to captured the experimentally observed shake-table response. The model predicted the shake-table response of the isolators with an average absolute error that ranged between 17.2-28.1% and 5.5-7.4% for the maximum displacements and accelerations, respectively. When the same results are statistically validated, the CDF curves match well, with the numerical being inside the 95% confidence interval of the experimental one, and the p-value always being higher than 0.33.

The conclusions of the present study are linked to the adopted testing conditions and approximations. Therefore, the following topics are open to further research:

(a) Lateral cyclic tests under higher velocities need to be performed to further investigate the behavior of the proposed isolator and obtain a detailed description of the velocity dependency of μ_{roll}.
(b) The system-level response of a seismically-isolated masonry dwelling supported on the proposed deformable rolling isolators, including three-dimensional earthquake excitation, remains to be quantified. In this system-level shake-table investigation, the finite strength, the flexibility, and the detailed geometrical characteristics of the superstructure should also be accounted for.
(c) In all tests that were performed in 1:2 scale, similitude of geometry, stresses, forces and time is preserved. The potential scale-dependence of the material properties of rubber is ignored. Therefore, further full-scale studies are needed to evaluate the existence of scale effects of rolling rubber isolators.
(d) Alternative variations of the isolator, with a thinner layer of rubber, could be used so that the behavior of the isolator can be approximated by a bilinear model. This would simplify the design procedure.
(e) Even though PU is not particularly susceptible to environmental corrosion (Konstantinidis, Kelly, and Makris 2008), the long-term behavior and degradation of the isolator under environmental conditions should be quantified to guarantee that the proposed bearings remain reliable after many years of service.

Acknowledgments

The isolator device discussed in this paper was brought to the attention of the senior author of this paper by Professor Michael Constantinou, who encouraged him to study this problem, including looking at flat rolling isolators. This interaction is gratefully acknowledged. The MS students Mr. Miro Chollet and Mr. Stefan Eyyi are kindly acknowledged for their technical assistance during the conduction of the experiments. Financial support to the authors was provided by the European Research Council (ERC) under Starting Grant 803908. The methods, results, opinions, findings, and conclusions presented in this report are those of the authors and do not necessarily reflect the views of the funding agency.

Disclosure statement

No potential conflict of interest was reported by the author(s).

Funding

The work was supported by the European Research Council [803908].

References

Almazán, J. L., and J. C. de la Llera. 2003. Accidental torsion due to overturning in nominally symmetric structures isolated with the FPS. *Earthquake Engineering & Structural Dynamics* 32 (6): 919–48. doi: 10.1002/eqe.255.

Bachmann, J. A., M. Strand, M. F. Vassiliou, M. Broccardo, and B. Stojadinović. 2018. Is rocking motion predictable? *Earthquake Engineering & Structural Dynamics* 47 (2): 535–52. doi: 10.1002/eqe.2978.

Bachmann, H., T. Wenk, M. Baumann, and P. Lestuzzi. 1999. Der neue ETH-Erdbebensimulator. *Schweizer Ingenieur und Architekt* 4: 63–67.

Brito, M. B., M. Akiyama, Y. Ichikawa, H. Yamaguchi, R. Honda, and N. Ishigaki. 2020. Bidirectional shaking table tests of a low-cost friction sliding system with flat-inclined surfaces. *Earthquake Engineering & Structural Dynamics* 49 (8): 817–37. doi: 10.1002/eqe.3266.

Brito, M. B., M. Akiyama, T. Seto, R. Honda, and N. Ishigaki. 2021. Shaking table test of a friction sliding system on a concrete member with variable curvature fabricated by a three-dimensional printer. *Journal of Earthquake Engineering* 26 (16): 8332–58. doi: 10.1080/13632469.2021.1991515.

Brito, M. B., H. Ishibashi, and M. Akiyama. 2019. Shaking table tests of a reinforced concrete bridge pier with a low-cost sliding pendulum system. *Earthquake Engineering & Structural Dynamics* 48 (3): 366–86. doi: 10.1002/eqe.3140.

Cilsalar, H., and M. C. Constantinou. 2019a. Behavior of a spherical deformable rolling seismic isolator for lightweight residential construction. *Bulletin of Earthquake Engineering* 17 (7): 4321–45. doi: 10.1007/s10518-019-00626-z.
Cilsalar, H., and M. C. Constantinou. 2019b. Development and validation of a seismic isolation system for lightweight residential construction. Technical Report MCEER. Report No.19-0001
Cilsalar, H., and M. C. Constantinou. 2020. Parametric study of seismic collapse performance of lightweight buildings with spherical deformable rolling isolation system. *Bulletin of Earthquake Engineering* 18 (4): 1475–98. doi: 10.1007/s10518-019-00753-7.
Constantinou, M. C., A. S. Mokha, and A. M. Reinhorn. 1990. Teflon bearings in base isolation II: Modeling. *Journal of Structural Engineering* 116 (2): 455–74. doi: 10.1061/(ASCE)0733-9445(1990)116:2(455).
Constantinou, M. C., A. S. Mokha, and A. M. Reinhorn. 1991. Study of sliding bearing and helical-steel-spring isolation system. *Journal of Structural Engineering* 117 (4): 1257–75. doi: 10.1061/(ASCE)0733-9445(1991)117:4(1257).
Cui, S., M. Bruneau, and M. C. Constantinou. 2012. Integrated design methodology for isolated floor systems in single-degree-of-freedom structural fuse systems. Technical Report MCEER. Report No. 12-0004
Das, A., S. K. Deb, and A. Dutta. 2016. Shake table testing of un-reinforced brick masonry building test model isolated by U-FREI. *Earthquake Engineering & Structural Dynamics* 45 (2): 253–72. doi: 10.1002/eqe.2626.
De Domenico, D., D. Losanno, and N. Vaiana. 2023. Experimental tests and numerical modeling of full-scale unbonded fiber reinforced elastomeric isolators (UFREIs) under bidirectional excitation. *Engineering Structures* 274. doi: 10.1016/j.engstruct.2022.115118.
Diani, J., B. Fayolle, and P. Gilormini. 2009. A review on the mullins effect. *European Polymer Journal* 45 (3): 601–12. doi: 10.1016/j.eurpolymj.2008.11.017.
Dormand, J. R., and P. J. Prince. 1980. A family of embedded Runge-kutta formulae. *Journal of Computational and Applied Mathematics* 6 (1): 19–26. doi: 10.1016/0771-050X(80)90013-3.
Eldredge, K. R., and D. Tabor. 1955. The mechanism of rolling friction I. The plastic range. *Proceedings of the Royal Society A* 229: 1177.
EN 1015-11. 1993. *Methods of test for mortar for masonry – Part 11: Determination of flexural and compressive strength of hardened mortar*. Brussels, Belgium: European Committee for Standardization.
FEMA P695. 2009. *Quantification of building seismic performance factors*. Washington, D.C., USA: Federal Emergency Management Agency.
Fink, K., E. Jensen, D. Mix, A. A. Taflanidis, and T. L. Kijewski-Correa. 2017. Mitigating seismic risk in the developing world: Lessons learned in Haiti and promotion of alternative solutions. 16th World Conference on Earthquake Engineering, 16WCEE, Santiago, Chile.
Foti, D. 2019. Rolling devices for seismic isolation of lightweight structures and equipment. Design and realization of a prototype. *Structural Control & Health Monitoring* 26 (3): e2311. doi: 10.1002/stc.2311.
Foti, D., and J. M. Kelly. 1996. Experimental analysis of a model isolated at the base with rubber-layer roller bearings (RLRB). *European Earthquake Engineering* 10: 3–13.
Harvey, P. S. 2016. Vertical accelerations in rolling isolation systems: Experiments and simulations. *Journal of Engineering Mechanics* 142 (3): 04015091. doi: 10.1061/(ASCE)EM.1943-7889.0001017.
Harvey, P. S., and H. P. Gavin. 2014. Double rolling isolation systems: A mathematical model and experimental validation. *International Journal of Non-Linear Mechanics* 61: 80–92. doi: 10.1016/j.ijnonlinmec.2014.01.011.
Harvey, P. S., and K. C. Kelly. 2016. A review of rolling-type seismic isolation: Historical development and future directions. *Engineering Structures* 125: 521–31. doi: 10.1016/j.engstruct.2016.07.031.
Harvey, P. S., G. P. Zéhil, and H. P. Gavin. 2014. Experimental validation of a simplified model for rolling isolation systems. *Earthquake Engineering & Structural Dynamics* 43 (7): 1067–88. doi: 10.1002/eqe.2387.
Ipek, C., E. D. Wolff, and M. C. Constantinou. 2021. Accuracy of analytical models to predict primary and secondary system response in seismically isolated buildings. *Soil Dynamics and Earthquake Engineering* 150: 106944. doi: 10.1016/j.soildyn.2021.106944.
Jampole, E. A., G. Deierlein, E. Miranda, B. Fell, S. Swensen, and C. Acevedo. 2016. Full-scale dynamic testing of a sliding seismically isolated unibody house. *Earthquake Spectra* 32 (4): 2245–70. doi: 10.1193/010616EQS003M.
Jampole, E. A., S. D. Swensen, B. Fell, E. Miranda, and G. G. Deierlein. 2014. Dynamic testing of a low-cost sliding isolation system for light-frame residential structures. *10NCEE*, Anchorage, Alaska.
Jangid, R. S., and Y. B. Londhe. 1998. Effectiveness of elliptical rolling rods for base isolation. *Journal of Structural Engineering* 124 (4): 469–72. doi: 10.1061/(ASCE)0733-9445(1998)124:4(469).
Katsamakas, A. A., G. Belser, M. F. Vassiliou, and M. Blondet. 2022. Experimental investigation of a spherical rubber isolator for use in low income countries. *Engineering Structures* 1 250: 113522. doi: 10.1016/j.engstruct.2021.113522.
Katsamakas, A. A., G. Belser, M. F. Vassiliou, M. Blondet, and B. Stojadinovic. 2021a. Experimental investigation of spherical rubber seismic isolation bearings. COMPDYN 8th ECCOMAS Thematic Conference on Computational Methods in Structural Dynamics and Earthquake Engineering, Athens, Greece.
Katsamakas, A. A., M. Chollet, S. Eyyi, and M. F. Vassiliou. 2021b. Feasibility study on re-using tennis balls as seismic isolation bearings. *Frontiers in Built Environment* 7. doi: 10.3389/fbuil.2021.768303.
Kelly, J. M., and A. Calabrese. 2012. Mechanics of fiber reinforced bearings. Berkeley, USA. PEER Report 101.

Kelly, J. M., and S. M. Takhirov. 2001. Analytical and experimental study of fiber-reinforced elastomeric isolator. PEER Report.

Kolmogorov, A. 1933. Sulla determinazione empirica di una lgge di distribuzione. *Institution Italian Attuari, Giorn* 4: 83–91.

Konstantinidis, D., and J. M. Kelly. 2012. Two low-cost seismic isolation systems. 15th World Conference on Earthquake Engineering, Lisbon, Portugal, 24–28.

Konstantinidis, D., J. M. Kelly, and N. Makris. 2008. Experimental investigations on the seismic response of bridge bearings. Earthquake Engineering Research Center, Report No. EERC 2008-03

Lee, G., Y. C. Ou, T. Niu, J. Song, and Z. Liang. 2010. Characterization of a roller seismic isolation bearing with supplemental energy dissipation for highway bridges. *Journal of Structural Engineering* 136 (5): 502–10. doi: 10.1061/(ASCE)ST.1943-541X.0000136.

Lin, T. W., and C. C. Hone. 1993. Base isolation by free rolling rods under basement. *Earthquake Engineering & Structural Dynamics* 22 (3): 261–73. doi: 10.1002/eqe.4290220307.

MATLAB. 2022. *High-performance language software for technical computation*. Natick, MA: The MathWorks, Inc.

Menga, N., F. Bottiglione, and G. Carbone. 2019. The non-linear dynamic behavior of a Rubber-Layer Roller Bearing (RLRB) for vibration isolation. *Journal of Sound and Vibration* 463: 114952. doi: 10.1016/j.jsv.2019.114952.

Menga, N., D. Foti, and G. Carbone. 2017. Viscoelastic frictional properties of rubber-layer roller bearings (RLRB) seismic isolators. *Meccanica* 52 (11): 2807–17. doi: 10.1007/s11012-016-0612-y.

Mullins, L. 1969. Softening of rubber by deformation. *Rubber Chemistry and Technology* 42 (1): 339–62. doi: 10.5254/1.3539210.

Nagarajaiah, S., A. M. Reinhorn, and M. C. Constantinou. 1991. Nonlinear dynamic analysis of 3-D-Base-isolated structures. *Journal of Structural Engineering* 117 (7): 2035–54. doi: 10.1061/(ASCE)0733-9445(1991)117:7(2035).

Norma Cubana NC46. 2017. *Construcciones sismorresistentes — requisitos basicos para el diseno y construccion*. Oficina Nacional de Normalizacion.

Osgooei, P. M., M. J. Tait, and D. Konstantinidis. 2014. Finite element analysis of unbonded square fiber-reinforced elastomeric isolators (FREIs) under lateral loading in different directions. *Composite Structures* 113: 164–73. doi: 10.1016/j.compstruct.2014.02.033.

Ou, Y. C., J. Song, and G. C. Lee. 2010. A parametric study of seismic behavior of roller seismic isolation bearings for highway bridges. *Earthquake Engineering & Structural Dynamics* 39: 541–59. doi: 10.1002/eqe.958.

Ruano, P. C., and A. Strauss. 2018. An experimental study on unbonded circular fiber reinforced elastomeric bearings. *Engineering Structures* 177: 72–84. doi: 10.1016/j.engstruct.2018.09.062.

Russo, G., M. Pauletta, and A. A. Cortesia. 2013. A study on experimental shear behavior of fiber-reinforced elastomeric isolators with various fiber layouts, elastomers and aging conditions. *Engineering Structures* 52: 422–33. doi: 10.1016/j.engstruct.2013.02.034.

Shampine, L. F., and M. W. Reichelt. 1997. The MATLAB ODE suite. *SIAM Journal on Scientific Computing* 18 (1): 1–22. doi: 10.1137/S1064827594276424.

Smirnoff, N. 1939. Sur les écarts de la courbe de distribution empirique. *Matematicheskii Sbornik* 48 (1): 3–26.

Somarathna, H. M., S. N. Raman, D. Mohotti, A. A. Mutalib, and K. H. Badri. 2020. Rate dependent tensile behavior of polyurethane under varying strain rates. *Construction and Building Materials* 10 254: 119203. doi: 10.1016/j.conbuildmat.2020.119203.

Swensen, S. 2014. Seismically Enhanced Light-Frame Residential Structures. Ph.D. Thesis, Stanford, CA: Stanford University

Tabor, D. 1955. The mechanism of rolling friction II. The elastic range. *Proceedings of the Royal Society A* 229:1177.

Toopchi□nezhad, H., M. J. Tait, and R. G. Drysdale. 2009. Shake table study on an ordinary low-rise building seismically isolated with SU-FREIs (stable unbonded-fiber reinforced elastomeric isolators). *Earthquake Engineering & Structural Dynamics* 38 (11): 1335–57. doi: 10.1002/eqe.923.

Tran, C., A. Calabrese, M. F. Vassiliou, and S. Galano. 2020. A simple strategy to tune the lateral response of unbonded Fiber Reinforced Elastomeric Isolators (FREIs). *Engineering Structures* 222: 111128. doi: 10.1016/j.engstruct.2020.111128.

Tsiavos, A., N. A. Alexander, A. Diambra, E. Ibraim, P. J. Vardanega, A. Gonzalez-Buelga, and A. Sextos. 2019. A sand-rubber deformable granular layer as a low-cost seismic isolation strategy in developing countries: Experimental investigation. *Soil Dynamics and Earthquake Engineering* 125: 105731. doi: 10.1016/j.soildyn.2019.105731.

Tsiavos, A., P. Haladij, A. Sextos, and N. A. Alexander. 2020a. Analytical investigation of the effect of a deformable sliding layer on the dynamic response of seismically isolated structures. *Structures* 27: 2426–36. doi: 10.1016/j.istruc.2020.08.016.

Tsiavos, A., A. Sextos, A. Stavridis, M. Dietz, L. Dihoru, and N. A. Alexander. 2020b. Large-scale experimental investigation of a low-cost PVC 'sand-wich'(pvc-s) seismic isolation for developing countries. *Earthquake Spectra* 36 (4): 1886–911. doi: 10.1177/8755293020935149.

Tsiavos, A., A. Sextos, A. Stavridis, M. Dietz, L. Dihoru, F. Di Michele, and N. A. Alexander. 2021. Low-cost hybrid design of masonry structures for developing countries: Shaking table tests. *Soil Dynamics and Earthquake Engineering* 146: 106675. doi: 10.1016/j.soildyn.2021.106675.

Tsopelas, P., and M. C. Constantinou. 1997. Study of elastoplastic bridge seismic isolation system. *Journal of Structural Engineering* 123 (4): 489–98. doi: 10.1061/(ASCE)0733-9445(1997)123:4(489).

Van Engelen, N. C., D. Konstantinidis, and M. J. Tait. 2016. Structural and nonstructural performance of a seismically isolated building using stable unbonded fiber-reinforced elastomeric isolators. *Earthquake Engineering & Structural Dynamics* 45 (3): 421–39. doi: 10.1002/eqe.2665.

Van Engelen, N. C., M. J. Tait, and D. Konstantinidis. 2014. Model of the shear behavior of unbonded fiber-reinforced elastomeric isolators. *Journal of Structural Engineering* 141 (7): 04014169. doi: 10.1061/(ASCE)ST.1943-541X.0001120.

Wasserman, L. 2004. *All of statistics: A concise course in statistical inference*, Vol. 26. New York: Springer.

Weißenborn, O., C. Ebert, and M. Gude. 2016. Modelling of the strain rate dependent deformation behaviour of rigid polyurethane foams. *Polymer Testing* 1 54: 145–49. doi: 10.1016/j.polymertesting.2016.07.007.

Wen, Y. K. 1975. Approximate method for non-linear random vibration. *Journal of the Engineering Mechanics Division* 102 (4): 389–401. doi: 10.1061/JMCEA3.0002029.

Yim, C. S., A. K. Chopra, and J. Penzien. 1980. Rocking response of rigid blocks to earthquakes. *Earthquake Engineering & Structural Dynamics* 8 (6): 565–87. doi: 10.1002/eqe.4290080606.

Zéhil, G. P., and H. P. Gavin. 2013. Simplified approaches to viscoelastic rolling resistance. *International Journal of Solids and Structures* 15 50 (6): 853–62. doi: 10.1016/j.ijsolstr.2012.09.025.

Zéhil, G. P., and H. P. Gavin. 2014. Rolling resistance of a rigid sphere with viscoelastic coatings. *International Journal of Solids and Structures* 1 51 (3–4): 822–38. doi: 10.1016/j.ijsolstr.2013.11.009.

Zhou, Q., X. Lu, Q. Wang, D. Feng, and Q. Yao. 1998. Dynamic analysis on structures base-isolated by a ball system with restoring capacity. *Earthquake Engineering & Structural Dynamics* 27 (8): 773–91. doi: 10.1002/(SICI)1096-9845(199808)27:8<773:AID-EQE749>3.0.CO;2-A.